

Available online at www.sciencedirect.com

ScienceDirect

journal homepage: www.elsevier.com/locate/he

Review Article

Perovskite-based proton conducting membranes for hydrogen separation: A review

Siti Salwa Hashim ^a, Mahendra Rao Somalu ^b, Kee Shyuan Loh ^b,
Shaomin Liu ^c, Wei Zhou ^d, Jaka Sunarso ^{a,*}

^a Faculty of Engineering, Computing and Science, Swinburne University of Technology, Jalan Simping Tiga, 93350, Kuching, Sarawak, Malaysia

^b Fuel Cell Institute, Universiti Kebangsaan Malaysia, 43600, Bangi, Selangor, Malaysia

^c Department of Chemical Engineering, Curtin University, Perth, WA, 6102, Australia

^d Jiangsu National Synergetic Innovation Center for Advanced Materials (SICAM), State Key Laboratory of Materials-Oriented Chemical Engineering, College of Chemical Engineering, Nanjing Tech University, No. 5 Xin Mofan Road, Nanjing, 210009, PR China

ARTICLE INFO

Article history:

Received 9 April 2018

Received in revised form

7 June 2018

Accepted 8 June 2018

Available online xxx

Keywords:

Hydrogen separation

Membrane

Perovskite

Proton conducting

ABSTRACT

Hydrogen is considered a fuel of the future due to its diversified supply and zero greenhouse gas emission. The application of advanced membrane technology for hydrogen separation within the larger hydrogen production process context can substitute the use of more expensive and energy intensive cryogenic distillation and pressure swing adsorption technologies. This review overviews the basic aspects and progresses in perovskite-based proton conducting hydrogen separation membranes. Different configurations such as symmetric, asymmetric, hollow fiber, and surface modified perovskite membranes with various compositions are discussed and summarized. The challenges and future directions of such membranes are also elaborated.

© 2018 Hydrogen Energy Publications LLC. Published by Elsevier Ltd. All rights reserved.

Contents

Introduction	00
Perovskite structure	00
Transport mechanisms	00
Hydration and proton concentration	00
Intrinsic defects and doping	00
Ambipolar transport and hydrogen flux	00
Current status	00
Disk-shaped membranes	00

* Corresponding author.

E-mail addresses: baryjakasunarso@yahoo.com, jsunarso@swinburne.edu.my (J. Sunarso).

<https://doi.org/10.1016/j.ijhydene.2018.06.045>

0360-3199/© 2018 Hydrogen Energy Publications LLC. Published by Elsevier Ltd. All rights reserved.

Single-phase membranes	00
Dual-phase membranes	00
Asymmetric membranes	00
Hollow fiber membranes	00
Surface-modified membranes	00
Challenges and outlook	00
Limitations	00
Future insights	00
Conclusions	00
Acknowledgment	00
References	00

Introduction

Over 60 million tons of hydrogen is produced per year for use in the chemical and refinery industries [1]. Hydrogen share in the energy market is increasing with the implementation of fuel cell systems and the growing demand for zero-emission fuels. Fuel cell electric vehicles (FCEVs) are powered by hydrogen and have the potential to revolutionize the transportation system. The northern German state of Schleswig-Holstein, for example, has declared plans to electrify its entire rail network by 2025, adopting fuel cell technology to power grids and also trains [2]. Plans are also in progress to realize hydrogen's potential in stationary applications. The United Kingdom City of Leeds has revealed its plan to become 'hydrogen city' in which the natural gas that runs through the city's pipes would be switched to hydrogen [3]. Japan has also announced plans to spend 40 billion yen to implement hydrogen technologies in the run up to the Tokyo 2020 Olympics [4]. As a part of the scheme, pipelines will be built that run through the athletes' village, delivering hydrogen to the industrial-scale fuel cells to power buildings [5].

Although hydrogen production technologies using renewable resources have been developed to achieve a sustainable energy cycle, hydrogen is still mainly produced from fossil sources due to technical and economical limitations of the existing technologies. In the near future, increased hydrogen production would likely be met via natural gas reforming [6]. Nevertheless, a large amount of carbon dioxide that is released during the hydrogen production from fossil fuels requires subsequent carbon dioxide capture and sequestration. Within this context, the development of hydrogen separation technologies remains one of the main spotlights that enables simultaneous high-purity hydrogen production and carbon dioxide capture. Pressure swing adsorption (PSA) and cryogenic distillation are currently being employed for hydrogen separation and recovery [7]. The PSA process relies on the adsorbents capacity to adsorb more impurities at high gas partial pressure than at low gas partial pressure. It offers the capability to produce very high purity hydrogen with up to 99.999% purity. Nevertheless, the PSA is only practical for medium and large industrial scale. The cryogenic distillation process is a sub-zero temperature separation process, which is based upon the difference in the boiling temperatures of the

feed components. Due to its high capital cost, the cryogenic distillation is only suitable for continuous and large-scale operation. The purity levels of hydrogen are limited to 90–98% [8].

Advanced membrane technology, on the other hand, allows hydrogen recovery from low purity or low-pressure hydrogen containing stream that is uneconomical otherwise via PSA or cryogenic technologies. Its low capital cost, low energy consumption, and ease of operation make membrane technology attractive, even for low gas volume case. Polymeric membranes are usually made from glassy polymers (e.g., cellulose acetate and polysulfone), deriving their selectivity by discriminating between penetrants' components with subtle differences in size. They are used in the industry to recover hydrogen from hydrocarbon streams, such as refinery off-gases. Nevertheless, the polymeric membranes cannot withstand high temperatures, high pressures, and aggressive chemical environments. High pressures can cause compaction of the polymer that reduces permeability, or even the collapse of hollow fibers.

Inorganic membranes have in general higher flux performances than polymeric membranes that warrant their potential use for hydrogen separation at high temperatures, apart from their superior chemical and thermal stability. The inorganic membranes for hydrogen separation and purification can be classified into two main groups, i.e., (1) porous membranes such as silicas, zeolites, and carbon; and (2) dense membranes that comprise both dense and composite metal and ceramic membranes. Porous ceramic membranes possess high permeability, moderate to high selectivity, and are chemically and thermally stable. These qualities are attractive for hydrogen separation application. Porous membranes generally rely on molecular sieving effect of small pores (3–4 Å) to separate hydrogen from other gases (e.g., N₂, CO₂, etc.). Hydrogen fluxes through these membranes are promising when the operating temperatures are between 200 °C and 600 °C. Amorphous silica membranes have achieved reasonable combinations of hydrogen permeability and selectivity [9]. There are however many issues to be resolved before silica membranes can be fully applied such as the limited structure stability in atmospheres containing steam. Zeolite membranes have better thermal stability in the presence of steam than non-doped amorphous silica membranes due to their crystalline structure. Nevertheless, they have only moderate hydrogen selectivity given their large porous

channels, which cannot provide molecular sieving effect [10]. Gas separation on zeolite membrane is mainly achieved via different gases adsorption affinity on its surface. Carbon membranes can be used in non-oxidizing environments between 500 °C and 900 °C. However, they are brittle and require special handling [11]. Besides its high price, the optimum manufacturing conditions for carbon membranes are yet to be determined.

Dense metallic membranes especially palladium and palladium alloys is a good alternative if highly pure hydrogen is required [12,13]. The hydrogen transport through the membrane occurs via the solution-diffusion mechanism, i.e., hydrogen is adsorbed on one side of the membrane, splits into two atoms, diffuses through the metal matrix, and recombines and desorbs at the permeate side. The asymmetric thin film configuration, i.e., thin dense metal layers deposited on porous ceramic or metallic supports is usually adopted to improve the hydrogen fluxes and reduce the membrane cost. The operating temperature of palladium membranes are between 300 °C and 500 °C. Hydrogen exposure at lower temperature nonetheless can damage these membranes since hydrogen is likely to be retained (frozen) within the palladium lattice. This can be circumvented by doping palladium with other metals such as silver or copper [13]. Palladium membranes have a major drawback in terms of their high sensitivity to chemicals such as sulfur, chlorine, and carbon monoxide that can poison the membrane surface. This poisoning effect can reduce the effective hydrogen fluxes by 20% up to 100%. Their commercial availability is still limited despite the intensive research and development efforts.

In dense ceramic membranes case, hydrogen is transported by means of coupled transport of protons and (charge compensating) electrons or electron holes, i.e., hydrogen permeability is thus dependent on the conductivities of the protons and the electronic species. This is unlike the metals and porous membranes cases, in which hydrogen diffuses through atomic or molecular hydrogen. Assuming that these

dense ceramic membranes are defect-free, they potentially offer 100% hydrogen selectivity (i.e., an infinite separation factor), chemical and mechanical stability at high temperatures, and low manufacturing cost with the operating temperature between 500 °C and 900 °C. Mixed protonic-electronic conducting ceramic materials of perovskite type have been identified as promising candidate for hydrogen separation membranes. Iwahara et al. [14] were the first to discover mixed protonic-electronic conduction in perovskite type ceramics at high temperatures (>500 °C) in a hydrogen-containing atmosphere. If identically high electronic conductivity could be simultaneously realized within these perovskites, their hydrogen permeability may be equivalent to those displayed by palladium and palladium-alloy membranes.

This review provides an overview of the perovskite-based mixed protonic-electronic conducting (MPEC) membranes for hydrogen separation. Doping strategies to improve the mixed protonic-electronic conductivity that correlates with the hydrogen permeation performance are summarized. The effects of various operating conditions and membrane configurations on the hydrogen permeation performance are also discussed. This review concludes by presenting the challenges and future directions of proton-conducting perovskite membranes for hydrogen separation.

Perovskite structure

Perovskite refers to the mixed oxides having the ideal crystal structure formula of ABO_3 (shown in Fig. 1). $SrTiO_3$ is a typical example. Perovskite framework consists of corner-shared BO_6 octahedra where the large A-site cation occupies the center of the cavity between 8 octahedra [15]. In perovskite compound, each B-site cation is surrounded by 6 O anions, forming 6 equidistant B–O bonds (Fig. 1(b)); and likewise, each A-site cation is surrounded by 12 O anions, forming 12 equidistant A–O bonds (Fig. 1(a)).

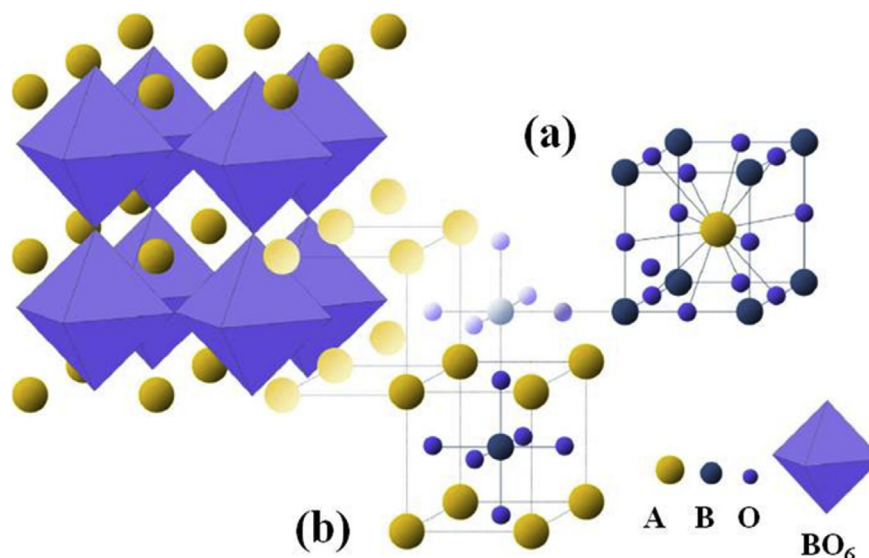


Fig. 1 – Different representations of a perovskite structure with (a) A-site cation occupies the center of the cube or (b) B-site cation occupies the center of the cube (Reproduced from [16]).

The effective valence state of A and B may vary as exemplified by the formula of $A^{2+}B^{4+}O_3$ or $A^{1+}B^{5+}O_3$ or $A^{3+}B^{3+}O_3$. A-site cation normally has larger size (1.10–1.80 Å) while B-site cation has medium size (0.62–1.00 Å). The A-site cation is surrounded by 12 oxygen anions while the B-site cation is surrounded by 6 oxygen anions [17,18]. A-site cation can be lanthanides (e.g., La, Pr, and Gd) or alkaline earth metals (e.g., Ba and Sr) while B site cation can be transition metals (e.g., Mn, Co, Ni, Cr, and Fe) or non-transition metals (e.g., Al and Ga) [18]. The Goldschmidt tolerance factor can be used to predict whether the cubic structure will form. The ionic radii values for metal cations compiled by Shannon and Prewitt [19], which were compiled using extensive amount of experimental data, have been widely used to predict Goldschmidt factor for new perovskite compositions. Table 1 shows several common A- and B-site cations of perovskites for hydrogen separation membranes. Details on the structure and properties of perovskites have been elaborated elsewhere [20–22].

Transport mechanisms

Hydration and proton concentration

Mixed protonic-electronic conductivity in electronic conducting perovskites is essentially created by the presence of substantial amount of oxygen vacancies that enables the formation of substantial amount of protons within the perovskite lattice. Such protons can exist from either a water vapor or a hydrogen-containing gas sources. In a humidified atmosphere, for example, the oxygen vacancy at the surface of proton conducting perovskite oxide becomes the active site for the water dissociation from the gas phase into a hydroxide ion and a proton (Fig. 2). The hydroxide ion subsequently fills the oxygen vacancy site while the proton attaches itself to the lattice oxygen via covalent bond and moves from one lattice oxygen site to another lattice oxygen site (Eq. (1)) [23]. The hydration of oxygen vacancies to form protons can be expressed as follows [24]:



In a dry hydrogen atmosphere, on the other hand, proton formation does not require the active role of oxygen vacancies along the membrane surface. The proton uptake to the lattice takes place via the formation of interstitial protons (Eq. (2)). The proton interacts with the electronic cloud of neighboring oxygen ion directly and attaches itself to the lattice oxygen (as in humidified atmosphere). The reaction is expressed as follows [26]:



where $V_O^{\bullet\bullet}$ is an oxygen vacancy with +2 oxidation state, O_O^{\times} is a neutral lattice oxygen, h^{\bullet} is an electron hole, and OH_O^{\bullet} is a

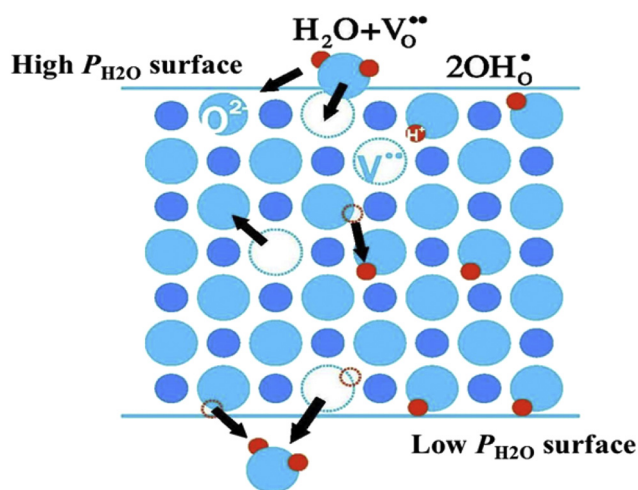


Fig. 2 – Proton transport in humidified atmosphere (Reproduced from [25]).

hydroxyl ion. The hydroxyl ion can be viewed as an interstitial proton that is attached to the lattice oxygen.

It should be noted that in both cases, the protons do not occupy lattice positions but are attached to the lattice oxygen ions forming OH_O^{\bullet} species. This is possible given their small sizes. The relationship between the electronic conductivity and the oxygen vacancies can be explained by considering the equilibrium relationships between oxygen vacancies and oxygen partial pressure as follows:



Eq. (3) becomes dominant at low oxygen partial pressure case whereby each generated oxygen vacancy is combined with two electrons while Eq. (4) is prevalent at high oxygen partial pressure case whereby the oxygen dissolves into the lattice. In the former case, the electron is the charge carrier while in the latter case, the electron hole is the charge carrier [27]. In humidified atmosphere for example, when the electron hole is present, the effect of water vapor on the conductivity can be rationalized by inspecting Eqs. (1) and (4). The incorporation of water vapor into the surface of perovskite oxide leads to the consumption of oxygen vacancies (Eq. (1)). This consumption simultaneously shifts the equilibrium of Eq. (4) from the product side towards the reactant side; thus, more oxygen vacancies are generated while the electron holes are depleted; resulting in the decrease in the electronic conductivity. Since the increase in protonic conductivity may not fully counterbalance such electronic conductivity decrease, the electrical conductivity is likely to decrease during such

Table 1 – Ionic radii for several common A- and B-site cations of perovskites [19].

Element	Sr ²⁺	Ba ²⁺	Y ³⁺	Ce ³⁺	Sm ³⁺	Eu ²⁺	Tb ³⁺	Tm ²⁺	Yb ²⁺
Coordination number	12	12	6	6	6	6	6	6	6
Ionic radius in (Å)	1.44	1.61	0.90	1.01	0.958	1.17	0.923	1.03	1.02

Table 2 – Ionic radii and electronegativity values for several common B-site doping elements in BaCeO₃^a [19,30]

Doping element	Ionic radii (Å) [19]	Electronegativity (neutral atom) [30]
Ce ⁴⁺	0.87	1.12
Zr ⁴⁺	0.72	1.33
Y ³⁺	0.90	1.22
Gd ³⁺	0.938	1.20
Pr ³⁺	0.99	1.13
Yb ³⁺	0.868	1.10
Sm ³⁺	0.958	1.17

^a All have coordination numbers of 6.

water incorporation. In humidified atmosphere, the increase of electrical conductivity with the increase in oxygen partial pressure is generally less apparent due to the development of proton conductivity [21].

For non-doped materials, the concentration of intrinsic defects is generally low in most cases, which translates to their low ionic conductivities. To enhance the ionic conductivity, the defect concentration in proton conductors can be modified via aliovalent doping (i.e., acceptor). Acceptor doping can be applied to increase the concentration of oxygen vacancies. This results in higher oxide ion conductivity and consequently, higher proton conductivity when the vacancies are hydrated using wet gas. The concentration of oxygen vacancies increases with increasing dopant concentration until the solubility limit of the dopant in the host oxide is reached. Still, at a particular dopant concentration, the interaction between different defects may occur; leading to the formation of defect association so that the conductivity may level off or even decrease with increase in the dopant concentration [28].

Intrinsic defects and doping

The best perovskites candidates in terms of high proton conductivities are doped BaCeO₃, BaZrO₃, SrCeO₃, and SrZrO₃. Among them, BaCeO₃-based oxides demonstrate the highest proton conductivity (i.e., $\sim 10^{-2}$ S cm⁻¹ at 700 °C). Nevertheless, they can easily decompose into barium carbonate and/or barium hydroxide in CO₂ and/or humid atmospheres [29]. Doping with cations having larger ionic radius than Ce were shown to increase the proton conductivity (relative to the non-doped compound). Doping with more electronegative dopants generally increases the structure stability [30]. Yttrium (Y) is one of the best co-dopant candidates since doping with either ytterbium (Yb) or praseodymium (Pr) tends to create mixed ionic-electronic conductivity (instead of

mixed protonic-electronic conductivity) [31,32]. An inspection into the ionic radii and electronegativity for several B-site cations indicates yttrium and gadolinium (Gd) as the ideal B-site dopants to partially replace Ce given their ionic radius proximity and substantially higher electronegativity (Table 2) [19,30]. Praseodymium, on the other hand, has significantly larger ionic radius that leads to structure instability while ytterbium has slightly smaller ionic radius size, both compared to cerium.

The electronic conductivity of doped SrCeO₃ correlates explicitly with the ionic potentials of the doping elements [21,22]. The electronic conduction in doped SrCeO₃ comes from the charge transfer between the two neighboring ions of different oxidation states. For pure SrCeO₃, the charge transfer between two Ce cations with different oxidation states can be represented by:



When Ce⁴⁺ is replaced by lower oxidation state cation (i.e., acceptor dopant) such as Tm³⁺, the oxygen vacancies and electronic holes are created. Some Tm²⁺ may also be converted to Tm³⁺ to maintain the charge neutrality. The following Eq. (6) represents the charge transfer between two Tm cations with different oxidation states:

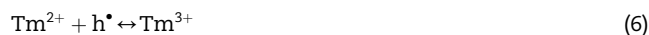


Table 3 compares the electrical conductivity (i.e., the sum of ionic conductivity and electronic conductivity) measured at 800 °C in pure oxygen for several doped SrCeO₃ oxides with the ionization potential of their dopant ions [21,33,34]. In pure oxygen, the electrical conductivity is effectively equal to the electronic conductivity [21]. The electronic conductivity increases with decreasing ionization potential (Table 3). SrCe_{0.95}Tm_{0.05}O_{3-δ} exhibits the lowest ionization potential and thus, the highest electronic conductivity of 1.29×10^{-2} S cm⁻¹ at 800 °C. This value is three orders of magnitude higher than SrCe_{0.95}Tb_{0.05}O_{3-δ} [33] and is an order of magnitude higher than SrCe_{0.95}Yb_{0.05}O_{3-δ} [34,35]. The improvement in electronic conductivity of these doped SrCeO₃ oxides therefore manifests into improved hydrogen permeation flux.

Ambipolar transport and hydrogen flux

Hydrogen transport in dense mixed protonic-electronic conducting (MPEC) perovskite membranes occurs through a different mechanism to the hydrogen transport in porous and metallic membranes. The transport of hydrogen from one side of the membrane to the other side is a sequence of several distinct processes. Hydrogen gas (and/or water vapor) on the feed side diffuses to the feed surface of the perovskite,

Table 3 – Comparison of the effect of different dopants on the electronic conductivity of SrCeO₃ at 800 °C in pure O₂ [21,33,34].

Materials	Ionization potential of the stable metal ions (eV)	Electronic conductivity (S cm ⁻¹)	References
Non-doped SrCeO ₃	36.8 (Ce ³⁺ → Ce ⁴⁺)	2.82×10^{-4}	[33]
SrCe _{0.95} Tb _{0.05} O _{3-δ}	39.8 (Tb ³⁺ → Tb ⁴⁺)	1.21×10^{-5}	[33]
SrCe _{0.95} Yb _{0.05} O _{3-δ}	25.0 (Yb ²⁺ → Yb ³⁺)	8.50×10^{-3}	[34]
SrCe _{0.95} Tm _{0.05} O _{3-δ}	23.7 (Tm ²⁺ → Tm ³⁺)	1.29×10^{-2}	[21]

followed by the adsorption and catalytic dissociation of hydrogen. A hydrogen atom usually loses its electron and becomes a protonic defect as it enters the perovskite lattice. The protonic defect then diffuses within the lattice to reach the other (permeate) surface. These protonic defects then recombine into hydrogen (and/or water vapor) on the permeate side of the membrane.

The proton and electron conductions across the membrane are driven by the conditions or processes that occur at the opposite surfaces of the membranes. For hydrogen separation, the driving force is a concentration gradient that can be represented by a Nernstian potential difference as follows:

$$E = -\frac{RT}{nF} \ln \left(\frac{P'_{H_2}}{P_{H_2}} \right) \quad (7)$$

where R is the universal gas constant, T is the temperature, n is the electron number in the hydrogen dissociation/association reaction (i.e., equal to 2), F is the Faraday constant, P_{H_2} is the hydrogen pressure in the feed side, and P'_{H_2} is the hydrogen pressure in the permeate side.

Under this potential difference, the dissociated protons and electrons move from the feed to the permeate side of the membrane. In MPEC membranes, protons do not originally present in the membrane structure. They are present as foreign species (i.e., defects) that are left behind from the synthesis process or are present in equilibrium with ambient hydrogen or water vapor [36]. Therefore, the chemical potentials of hydrogen and/or water vapor, temperature, and oxygen partial pressure should be precisely measured (or determined) under experimental conditions [21]. The membrane material on the hydrogen-containing feed side generally features both protonic and electronic conductivity. On the other hand, the permeate side of the membrane, in the start of the process, is exposed to either an inert or oxidizing gas. Therefore, the hydrogen permeability through the membrane under this condition is normally limited by the electronic conductivity. For example, an initially non-permeable MPEC membrane subjected to the hydrogen/argon and hydrogen/80% argon+20% oxygen gradients may become hydrogen permeable via an activated mixed-conducting mechanism that is created upon lowering the oxygen partial pressure in permeate side to a very low value. This can be achieved by introducing a low amount of other than hydrogen reducing gas such as carbon monoxide in the permeate side to create electronic conductivity and ultimately, mixed protonic-electronic conductivity across the membrane [37]. The flow of the reducing gas can then be stopped once hydrogen exists in the permeate side since hydrogen presence by then ensures high electronic conductivity across the membrane [37].

Hydrogen flux also increases with increasing upstream (feed) hydrogen partial pressure due to the larger driving force (between feed side and permeate side) [38]. The resultant increase in the concentrations of charge carriers on the feed side may additionally lead to the subsequent increase in the protonic and electronic conductivities of the membrane. Increasing the oxygen partial pressure on the permeate side may also increase the hydrogen flux due to the improved electronic conductivity and the higher driving force as observed in $\text{SrCe}_{0.95}\text{Tm}_{0.05}\text{O}_{3-\delta}$ case [21]. Whether the overall

transport across the membranes manifests into hydrogen and/or water permeation depends on the nature of the conduction properties of the material and the chemical potential gradient across it. In addition, for materials with mixed ionic-electronic conductivity, the contribution from water splitting must be accounted for flux measurements under wet sweep conditions, particularly when evaluating the concentration of different gaseous species in the outlet of the permeate side. The extent of the water splitting can be determined by measuring the ambipolar ionic-electronic conduction induced by the gradient in the oxygen partial pressure from the feed to the permeate side of the membrane [28].

Current status

Research and development efforts in perovskite-based hydrogen separation membranes that aims to improve their hydrogen permeability and stability can be organized into five major categories, i.e., (1) Optimization of single-phase perovskite composition; (2) Development of dual-phase perovskite membrane; (3) Fabrication of asymmetric structure; (4) Fabrication of hollow fiber-shaped membrane; and (5) Modification of membrane surface. The first and second approaches are segregated under a single relevant section since the performance evaluation of single-phase perovskite and dual-phase membranes are made using laboratory scale disk-shaped membrane.

Disk-shaped membranes

Disk membranes have been widely employed for fundamental research studies and screening of new membrane materials. The diameter of the disk is typically a few centimeters with the thicknesses of around 0.5–4.0 mm. The preparation of disk membranes consists of three sequential steps, i.e., powder synthesis and calcination, disk fabrication, and sintering. The synthesis and calcination process influences the particle size, the chemical composition homogeneity, and the sinterability of the powders. The most commonly used synthesis route is solid-state reactions of mixed oxides, carbonates, or salts [39,40]. The particle size is controlled by the nature of the mixing and grinding processes. Other powder synthesis routes include co-precipitation, sol-gel, and hydrothermal routes. Isostatic pressing step using pellet press die set is normally applied to compact the calcined powder into the so-called “green” disk. This “green” disk needs to be sintered at temperatures higher than the initial calcination temperature (above 1000 °C) to obtain a pore-free (dense) disk membrane. Readers interested in perovskite synthesis routes and disk-shaped membrane fabrication methods can find out more details elsewhere [41,42].

Single-phase membranes

Since Iwahara et al. [14] first reported the high protonic conductivity of doped SrCeO_3 perovskite oxides in hydrogen-containing atmospheres, these materials have been studied extensively as hydrogen separation membranes [21,37,43–47]. Further work proceeded in other doped perovskites such as $\text{BaCe}_{1-x}\text{M}_x\text{O}_{3-\delta}$ (M here represents rare earth elements) [48–51].

BaCeO₃-based perovskite oxides however exhibited oxygen ionic conductivity comparable to the proton conductivity [52], which limits their applications when oxygen is present. Therefore, SrCeO₃-based perovskites become more promising hydrogen separation membrane materials if their electronic conductivity can be improved via partial substitution (doping) with other metal dopants. The hydrogen permeation performances for several compositions of disk-shaped membranes are listed in Table 4 [21,37,43–51].

The introduction of Tb into the B-site of SrCeO₃ perovskite lattice decreased the electronic conductivity in air and in inert gas [37]. This is due to the higher fourth ionization potential of Tb (39.8 eV) compared to other trivalent cations (e.g., Yb or Tm) (Table 3) [33,34]. Wei et al. evaluated the hydrogen permeation fluxes of SrCe_{1-x}Tb_xO_{3-δ} (x = 0.025, 0.05, and 0.1) membranes under different sweep gases [37]. The use of Ar or a 20 vol% O₂ in Ar as the sweep gas resulted in non-detectable hydrogen permeation flux, irrespective of the Tb content in the compounds. This indicates the low electronic conductivities of the compounds (<10⁻⁴ S cm⁻¹) on the sweep side in Ar or O₂ and Ar mixtures [33]. By decreasing the oxygen partial

pressure to a certain level, the electronic conductivity of Tb-doped SrCeO₃-based perovskites could be effectively enhanced [53]. This was achieved by introducing a reducing gas into the system. When a 1 vol% CO and 99 vol% Ar mixture was utilized as the sweep gas, the hydrogen flux can be observed in which SrCe_{0.975}Tb_{0.025}O_{3-δ} exhibited the highest flux.

The synergistic effect of zirconium (Zr) for SrCeO₃-based membranes was revealed by Kniep and Lin [44]. In their work, Zr was doped to the B-site of SrCe_{0.95}Tm_{0.05}O_{3-δ} to form a series of SrCeO₃-based membranes with a composition of SrCe_{0.95-x}Zr_xTm_{0.05}O_{3-δ} (x = 0.00, 0.10, 0.20, 0.30, and 0.40). These compositions were prepared using a liquid citrate process and their lattice parameters, protonic and electronic conductivities, chemical stability, and hydrogen permeation properties were systematically evaluated as a function of the Zr content. Powder X-ray diffraction showed that all SrCe_{0.95-x}Zr_xTm_{0.05}O_{3-δ} compositions exhibit orthorhombic lattice. Furthermore, the lattice volume decreased with increasing Zr content because of the smaller ionic radius of six coordinated Zr⁴⁺ (0.72 Å) compared to Ce⁴⁺ (0.87 Å) [19], which

Table 4 – Disk-shaped proton conducting perovskite membranes performance overview for H₂ permeation [21,37,43–51].

Materials	H ₂ flux (mL cm ⁻² min ⁻¹)	Feed/sweep atmospheres	Temperature (°C)	Thickness (mm)	Note	Ref.
BaCe _{0.80} Y _{0.20} O _{3-δ}	0.01	50% H ₂ + 50% He/N ₂	950	1.00	Disk	[48]
BaCe _{0.95} Nd _{0.05} O _{3-δ}	0.017	Dry 80% H ₂ + 20% He/Dry 98% Ar + 2% Ne	925	0.70	Disk	[49]
BaCe _{0.95} Nd _{0.05} O _{3-δ}	0.026	80% H ₂ + 15% H ₂ O + 5% He/Dry 98% Ar + 2% Ne	925	0.70	Disk	[49]
BaZr _{0.9} Fe _{0.1} O _{3-δ}	0.75	20% H ₂ + 80% He/Ar	900	1.15	Disk	[50]
BaZr _{0.80} Y _{0.15} Mn _{0.05} O _{3-δ}	0.03	Wet 50% H ₂ + 50% He/Wet Ar	1000	0.90	Disk	[51]
SrCe _{0.95} Eu _{0.05} O _{3-δ}	4.28 × 10 ⁻³	Dry 100% H ₂ /He	850	1.72	Disk	[43]
SrCe _{0.95} Eu _{0.05} O _{3-δ}	3.88 × 10 ⁻³	Wet 100% H ₂ /He	850	1.72	Disk	[43]
SrCe _{0.95} Sm _{0.05} O _{3-δ}	3.13 × 10 ⁻³	Dry 100% H ₂ /He	850	1.72	Disk	[43]
SrCe _{0.95} Sm _{0.05} O _{3-δ}	1.62 × 10 ⁻³	Wet 100% H ₂ /He	850	1.72	Disk	[43]
SrCe _{0.95} Tb _{0.05} O _{3-δ}	1.4 × 10 ⁻²	20% H ₂ + 80% He/0.001 atm CO + Ar	900	1.00	Disk	[37]
SrCe _{0.95} Tb _{0.05} O _{3-δ}	1.6 × 10 ⁻²	20% H ₂ + 80% He/0.1 atm CO + Ar	900	1.00	Disk	[37]
SrCe _{0.95} Tm _{0.05} O _{3-δ}	0.04	10% H ₂ + 90% He/Air	900	1.60	Disk	[21]
SrCe _{0.95} Tm _{0.05} O _{3-δ}	4.25 × 10 ⁻²	10% H ₂ + 90% N ₂ /20% O ₂ + 80% Ar	900	1.60	Disk	[44]
SrCe _{0.95} Tm _{0.05} O _{3-δ}	9.54 × 10 ⁻³	25% H ₂ + 75% Ar/Ar	900	0.7	Disk	[45]
SrCe _{0.95} Tm _{0.05} O _{3-δ}	0.022	H ₂ /Ar	900	0.7	Disk	[45]
SrCe _{0.95} Yb _{0.05} O _{3-δ}	9.14 × 10 ⁻³	25% H ₂ + 75% Ar/Ar	900	0.7	Disk	[45]
SrCe _{0.95} Yb _{0.05} O _{3-δ}	0.019	H ₂ /Ar	900	0.7	Disk	[45]
SrCe _{0.95} Zr _{0.10} Tm _{0.05} O _{3-δ}	1.50 × 10 ⁻²	10% H ₂ + 90% N ₂ /20% O ₂ + 80% Ar	900	1.60	Disk	[44]
SrCe _{0.75} Zr _{0.2} Tm _{0.05} O _{3-δ}	0.042	40% H ₂ + 60% He/Ar	900	1.20	Disk	[46]
SrCe _{0.95} Tm _{0.05} O _{3-δ}	0.054	50% H ₂ + 50% He/Ar	900	1.20	Disk	[47]
SrCe _{0.85} In _{0.1} Tm _{0.05} O _{3-δ}	0.042	50% H ₂ + 50% He/Ar	900	1.20	Sol-gel	[47]
SrCe _{0.75} In _{0.2} Tm _{0.05} O _{3-δ}	0.033	50% H ₂ + 50% He/Ar	900	1.20	Sol-gel	[47]

also signifies uniform distribution of Zr and Ce in the lattice. The increase of Zr concentration impedes the electronic conductivity of $\text{SrCe}_{0.95-x}\text{Zr}_x\text{Tm}_{0.05}\text{O}_{3-\delta}$ due to the lower conductivity of zirconates. The gradual decrease of protonic conductivities at 900 °C from 0.0031 S cm^{-1} (for $x = 0.0$) to 0.0026 S cm^{-1} (for $x = 0.20$) manifests with an increase in Zr doping content. This shows that Zr doping content affects both protonic and electronic conductivities of $\text{SrCe}_{0.95-x}\text{Zr}_x\text{Tm}_{0.05}\text{O}_{3-\delta}$. Likewise, the hydrogen permeation decreased with increasing Zr content since it reduces the protonic and electronic conductivities. The hydrogen permeation of $\text{SrCe}_{0.95}\text{Tm}_{0.05}\text{O}_{3-\delta}$ ($x = 0.0$) membrane is about 5 times higher than that of $\text{SrCe}_{0.75}\text{Zr}_{0.20}\text{Tm}_{0.05}\text{O}_{3-\delta}$ ($x = 0.20$) membrane under the same experimental condition (750–900 °C). In a CO_2 -containing environment, $\text{SrCe}_{0.75}\text{Zr}_{0.20}\text{Tm}_{0.05}\text{O}_{3-\delta}$ ($x = 0.20$) membrane have a larger steady-state hydrogen permeation flux and superior chemical stability over $\text{SrCe}_{0.95}\text{Tm}_{0.05}\text{O}_{3-\delta}$ ($x = 0.0$) membrane.

Higher CO_2 resistance can be attained via partial replacement of cerium (Ce) with indium (In) in $\text{BaCeO}_{3-\delta}$ -based oxides [54,55]. Nevertheless, not much attention has been given to $\text{SrCeO}_{3-\delta}$ -based oxides. In this context, Yuan et al. reported that In doping into the B-site of $\text{SrCe}_{0.95}\text{Tm}_{0.05}\text{O}_{3-\delta}$ represented by $\text{SrCe}_{0.95-x}\text{In}_x\text{Tm}_{0.05}\text{O}_{3-\delta}$ ($x = 0.00, 0.05, 0.10, 0.15$, and 0.20) compositions improved the sintering activity of $\text{SrCe}_{0.95}\text{Tm}_{0.05}\text{O}_{3-\delta}$ membrane due to the presence of SrIn_2O_4 phase [47]. Powder X-ray diffraction patterns (Fig. 3) and scanning electron microscopy results (Fig. 4) revealed that an increase in the In content in the oxides causes lattice constriction and promotes grain growth during sintering process. The membrane stability test concurrently showed that In doping improved the chemical stability against CO_2 and the chemical stability increased with the increase of In content. Despite its improved sintering activity and CO_2 resistance, $\text{SrCe}_{0.95-x}\text{In}_x\text{Tm}_{0.05}\text{O}_{3-\delta}$ demonstrated a decrease in the hydrogen permeation with increasing In content under

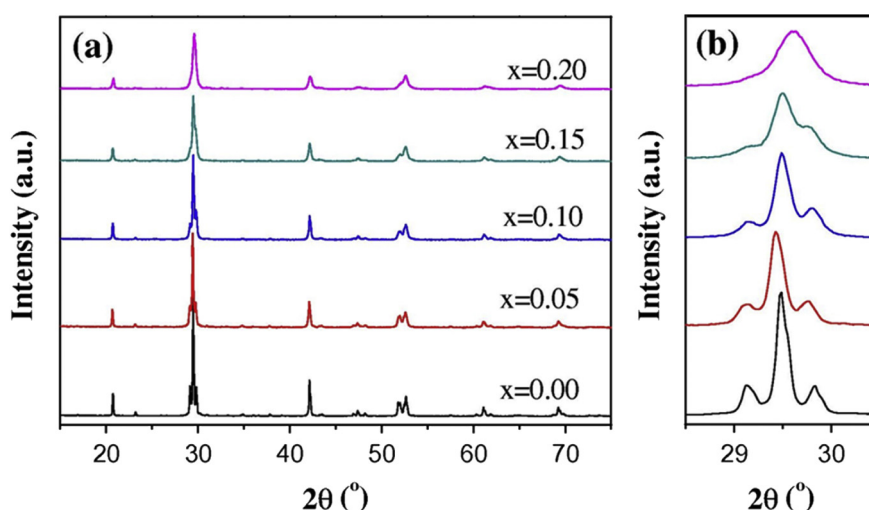


Fig. 3 – (a) Powder X-ray diffraction patterns of $\text{SrCe}_{0.95-x}\text{In}_x\text{Tm}_{0.05}\text{O}_{3-\delta}$ membranes calcined at 1300 °C for 10 h and (b) enlarged section at 2θ range of 28.5–30.5° (Reproduced from [47]).

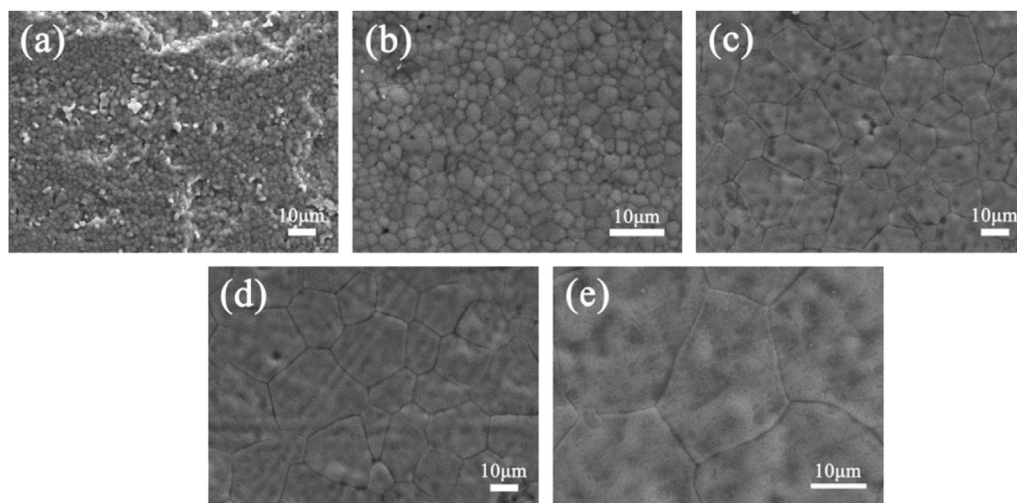


Fig. 4 – Scanning electron micrographs of $\text{SrCe}_{0.95-x}\text{In}_x\text{Tm}_{0.05}\text{O}_{3-\delta}$ membranes sintered at 1300 °C for 10 h (a) $x = 0.00$; (b) $x = 0.05$; (c) $x = 0.10$; (d) $x = 0.15$; and (e) $x = 0.20$ (Reproduced from [47]).

40% H₂–He/Ar gradient at 700–900 °C. Indium presence can thus be correlated to the decrease of the protonic conductivity of SrCe_{0.95–x}In_xTm_{0.05}O_{3–δ} membranes.

Tan and co-workers reported the hydrogen permeation flux of less than 0.01 mL cm^{–2} min^{–1} at 950 °C under 50 vol% H₂ and 50 vol% He in N₂ gradient for a 1 mm-thick disk-shaped BaCe_{0.8}Y_{0.2}O_{3–δ} membrane [48]. Another doped-BaCeO₃ of interest is Nd-doped BaCeO₃ (BaCe_{0.95}Nd_{0.05}O_{3–δ}) [49]. The BaCe_{0.95}Nd_{0.05}O_{3–δ} exhibited high protonic conductivity of up to 2.2×10^{-2} S cm^{–1} [38]. Chen et al. demonstrated that the conductivities of BaCe_{0.95}Nd_{0.05}O_{3–δ} under different atmospheres are very close to each other with a slight increase in the sequence of $\sigma(\text{Ar}) < \sigma(\text{air}) < \sigma(\text{O}_2)$ [56]. The hydrogen permeation fluxes through a 1-mm thick BaCe_{0.95}Nd_{0.05}O_{3–δ} membrane under wet conditions were higher than those measured under dry conditions (Fig. 5). A maximum hydrogen permeation flux of 0.02 mL cm^{–2} min^{–1} was obtained at 925 °C under wet condition [49]. Zhang and Wilhite reported that, relative to BaZrO₃, 10 mol% Fe-doped BaZrO₃ (BaZr_{0.9}Fe_{0.1}O_{3–δ}) has higher electronic conductivity due to valance changes from Fe²⁺/Fe³⁺ pair; resulting in an improved hydrogen permeability [50]. The hydrogen permeation fluxes reached as high as 0.75 mL cm^{–2} min^{–1} at 900 °C for a 1.15 mm-thick BaZr_{0.9}Fe_{0.1}O_{3–δ} membrane when 20 vol% H₂ in Ar and Ar were used in the feed and sweep side, respectively. The obtained fluxes increased with the decrease of membrane thickness; implying that the hydrogen permeation is bulk-diffusion limited. Between 600 °C and 700 °C, the hydrogen permeation of BaZr_{0.9}Fe_{0.1}O_{3–δ} membrane was limited by the electronic transport with high activation energy of 72–94 kJ mol^{–1}. Its hydrogen permeation was nonetheless limited by the mixed protonic-electronic transport with the low activation energy of 18–23 kJ mol^{–1} between 700 °C and 900 °C. They also demonstrated that the BaZr_{0.9}Fe_{0.1}O_{3–δ} membrane is both chemically and mechanically stable over dry and humidified hydrogen-containing environments [50]. Other than the study by Zhang and

Wilhite [50], no other works on BaZrO₃-based materials for hydrogen separation membranes are available.

Escalástico et al. prepared BaZr_{0.8}Y_{0.15}Mn_{0.05}O_{3–δ} membrane by mixing corresponding metal oxides in their stoichiometric proportions via ball-milling for 10 h followed by calcination at 1400 °C for 32 h and subsequent ball-milling for 1 day using zirconia balls [51]. The resulting powders were then pressed and sintered, resulting in 0.90-mm thick disks. Two hydration conditions were employed to investigate the effect of the humidification degree on the hydrogen flux of the BaZr_{0.8}Y_{0.15}Mn_{0.05}O_{3–δ} membrane, i.e., only the feed side is humidified and both feed and permeate sides are humidified. An increase in the hydrogen permeation flux can be observed when both feed and permeate sides were humidified. This can be ascribed to better hydration of the membrane especially in the region close to the permeate, which resulted into a higher proton concentration across the membrane. Moreover, the increase in the oxygen ion transport caused by the higher oxygen partial pressure gradient between the feed side and permeate side indicates the contribution of the water splitting in the permeate side. Note that the oxygen partial pressure gradient across the membrane and the associated oxygen ion transport direction are reversed when the permeate side is humidified.

Dual-phase membranes

Despite significant progress in the development of single-phase perovskite proton conducting membranes, the main challenge lies in the obtainment of materials that can exhibit simultaneously high electronic and proton conductivities. An alternative approach to resolve this issue involves combining two individual materials; one having high electronic conductivity and another having high proton conductivity; forming the so-called dual-phase or composite membranes such as ceramic-metallic (cermet) and ceramic-ceramic (cercer). The incorporation of a metal phase increases the electronic conductivity and also enhances the interfacial catalytic activities of the MPEC membranes [57]. The ceramic phase contributes its high mechanical strength to the composite which is lacking in the individual thin metallic (or alloy) membrane. Different combinations with respect to the functional properties of both ceramic and metallic phases can be realized via (1) combining a metal or an alloy having high hydrogen permeability with a ceramic having low hydrogen permeability; (2) combining a metal having low hydrogen permeability with a ceramic having high hydrogen permeability; or (3) combining a metal or an alloy having high hydrogen permeability with a ceramic having high hydrogen permeability. The hydrogen permeation performances of several cermet membranes are summarized in Table 5 [58–69].

Membranes based on the first combination that are composed of a hydrogen permeable metal such as palladium yielded the highest hydrogen flux. For example, the hydrogen permeation flux obtained through a 400 μm-thick dense Pd–BaCe_{0.4}Zr_{0.4}Gd_{0.1}Dy_{0.1}O_{3–δ} with 50 vol% Pd cermet membrane was 1.25 mL cm^{–2} min^{–1} in 50 vol% H₂ in CO₂ feed mixture at 700 °C [67]. Given the high palladium cost, another cheaper metal such as nickel, has been assessed as an alternative.

The hydrogen permeation flux through a membrane based on the second combination is generally higher than that through the single-phase membranes due to the presence of

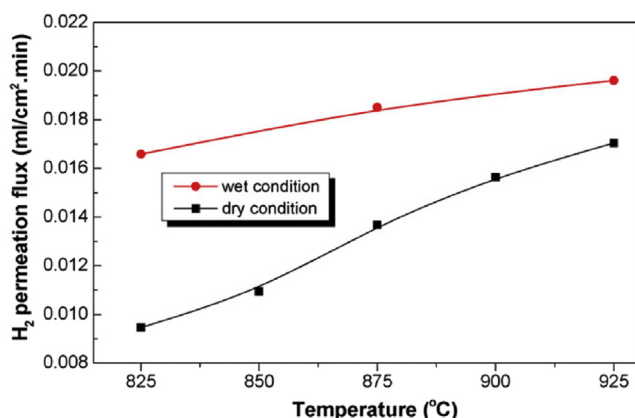


Fig. 5 – Temperature-dependent hydrogen permeation fluxes for BaCe_{0.95}Nd_{0.05}O_{3–δ} under dry and wet conditions. Membrane thickness: 0.7 mm. Feed side: dry condition = 80 mL min^{–1} H₂ + 20 mL min^{–1} He, wet condition = 80 mL min^{–1} H₂ + 15 mL min^{–1} He + 5 mL min^{–1} steam. Sweep side: 29.5 mL min^{–1} Ar + 0.5 mL min^{–1} Ne (Reproduced from [49]).

Table 5 – Dual-phase cermet proton conducting perovskite membranes performance overview for H₂ permeation [58–69].

Materials	H ₂ flux (mL cm ⁻² min ⁻¹)	Feed/sweep atmospheres	Temperature (°C)	Thickness (mm)	Note	Ref.
Ni–BaCe _{0.85} Tb _{0.05} Zr _{0.10} O _{3-δ} (50:50 wt%)	0.17	Dry 50% H ₂ + 50% He/Ar	800	0.50	Disk	[59]
Ni–BaCe _{0.90} Y _{0.10} O _{3-δ} (40:60 vol%)	0.76	Dry 4% H ₂ + 96% He/N ₂ + H ₂	800	0.40	Disk	[60]
Ni–BaZr _{0.10} Ce _{0.70} Y _{0.20} O _{3-δ} (40:60 vol%)	0.056	Wet 4% H ₂ + 96% He/N ₂ + H ₂	900	1	Disk	[61]
Ni–BaZr _{0.10} Ce _{0.70} Y _{0.20} O _{3-δ} (40:60 vol%)	0.15	Wet 40% H ₂ + 20% CO ₂ + 40% He/N ₂ + H ₂	900	0.75	Disk	[61]
Ni–BaZr _{0.10} Ce _{0.70} Y _{0.20} O _{3-δ} (40:60 vol%)	0.805	100% H ₂ /He	900	0.266	Disk	[62]
Ni–BaZr _{0.10} Ce _{0.70} Y _{0.20} O _{3-δ} (30:70 vol%)	3.36 × 10 ⁻²	40% H ₂ + 58.5% N ₂ + 1.5% H ₂ O/Ar	700	0.5	Disk	[63]
Ni–BaZr _{0.10} Ce _{0.70} Y _{0.20} O _{3-δ} (30:70 vol%)	2.68 × 10 ⁻²	40% H ₂ + 1.5% H ₂ O + N ₂ + 30 ppm H ₂ S/Ar	700	0.5	Disk	[63]
Ni–BaZr _{0.10} Ce _{0.70} Y _{0.20} O _{3-δ} (30:70 vol%)	2.35 × 10 ⁻²	40% H ₂ + 1.5% H ₂ O + N ₂ + 60 ppm H ₂ S/Ar	700	0.5	Disk	[63]
Ni–BaZr _{0.10} Ce _{0.70} Y _{0.10} Yb _{0.10} O _{3-δ} (40:60 vol%)	1.74 × 10 ⁻²	20% H ₂ + 80% He/N ₂	900	0.75	Disk	[64]
Ni–BaZr _{0.10} Ce _{0.70} Y _{0.10} Yb _{0.10} O _{3-δ} (40:60 vol%)	3.36 × 10 ⁻²	20% H ₂ + 5% CO ₂ + 75% He/N ₂	900	0.75	Disk	[64]
Ni–BaZr _{0.10} Ce _{0.70} Y _{0.10} Yb _{0.10} O _{3-δ} (40:60 vol%)	4.30 × 10 ⁻²	20% H ₂ + 40% CO ₂ + 40% He/N ₂	900	0.75	Disk	[64]
Ni–BaZr _{0.10} Ce _{0.70} Y _{0.10} Yb _{0.10} O _{3-δ} (40:60 vol%)	4.56 × 10 ⁻²	20% H ₂ + 60% CO ₂ + 20% He/N ₂	900	0.75	Disk	[64]
Ni–BaZr _{0.10} Ce _{0.70} Y _{0.10} Yb _{0.10} O _{3-δ} (40:60 vol%)	0.118	40% H ₂ + 57% He + 3% H ₂ O/N ₂	900	0.56	Disk	[58]
Ni–BaZr _{0.10} Ce _{0.70} Y _{0.10} Yb _{0.10} O _{3-δ} (40:60 vol%)	0.127	40% H ₂ + 10% CO ₂ + 47% He + 3% H ₂ O/N ₂	900	0.56	Disk	[58]
Ni–BaZr _{0.10} Ce _{0.70} Y _{0.10} Yb _{0.10} O _{3-δ} (40:60 vol%)	0.122	40% H ₂ + 20% CO ₂ + 37% He + 3% H ₂ O/N ₂	900	0.56	Disk	[58]
Ni–BaZr _{0.10} Ce _{0.70} Y _{0.10} Yb _{0.10} O _{3-δ} (40:60 vol%)	0.114	40% H ₂ + 30% CO ₂ + 27% He + 3% H ₂ O/N ₂	900	0.56	Disk	[58]
Ni–BaZr _{0.10} Ce _{0.70} Y _{0.10} Yb _{0.10} O _{3-δ} (40:60 vol%)	0.083	40% H ₂ + 40% CO ₂ + 17% He + 3% H ₂ O/N ₂	900	0.56	Disk	[58]
Ni–Ba _{0.8} Zr _{0.5} Ce _{0.035} Tb _{0.15} O _{3-δ} (40:60 vol%)	0.07	16.7% H ₂ + 83.3% N ₂ /Ar	900	1.5	Disk	[69]
Ni–BaZr _{0.70} Pr _{0.10} Y _{0.10} O _{3-δ} (40:60 vol%)	1.62 × 10 ⁻²	40% H ₂ + 57% N ₂ + 3% H ₂ O/Dry Ar	950	0.40	Disk	[65]
Pd–CaZr _{0.90} Y _{0.10} O _{3-δ} (50:50 vol%)	1.30	20% H ₂ + 80% He/Dry N ₂	900	0.55	Disk	[66]
Pd–CaZr _{0.90} Y _{0.10} O _{3-δ} (50:50 vol%)	2.30	80% H ₂ + 20% He/Dry N ₂	900	0.55	Disk	[66]
Pd–CaZr _{0.90} Y _{0.10} O _{3-δ} (50:50 vol%)	0.89	20% H ₂ + 30% CO ₂ + 50% He/Dry N ₂	900	0.47	Disk	[66]
Pd–BaCe _{0.40} Zr _{0.40} Gd _{0.10} Dy _{0.10} O _{3-δ} (50:50 vol%)	2.77	100% H ₂ /Dry N ₂	700	0.40	Disk	[67]
Pd–BaCe _{0.40} Zr _{0.40} Gd _{0.10} Dy _{0.10} O _{3-δ} (50:50 vol%)	1.25	50% H ₂ + 50% CO ₂ /Dry N ₂	700	0.40	Disk	[67]
Cu–BaZr _{0.9} Y _{0.1} O _{3-δ} (60:40 vol%)	4.6 × 10 ⁻⁴	100% H ₂ /Dry Ar	882	1.90	Disk	[68]
Molten Cu infiltration						

the metallic phase such as Ni that increases the overall electronic conductivity [60,62]. It is a typical anode catalyst in fuel cell with excellent chemisorption properties that can promote the catalytic surface reaction. Nickel has substantial chemical and thermal stability, but its thermal expansion of $13.4 \times 10^{-6} \text{ K}^{-1}$ is also close to that of $\text{BaCe}_{0.9}\text{Y}_{0.1}\text{O}_{3-\delta}$ (i.e., $11.7 \times 10^{-6} \text{ K}^{-1}$) [60]. Its relatively high melting point (i.e., 1453°C) furthermore makes it suitable for the typical sintering required for densification of proton conducting membranes at such high temperatures. Kim et al. employed the high-energy milling process to optimize the mixing scale and homogeneity of the $\text{Ni-BaCe}_{0.9}\text{Y}_{0.1}\text{O}_{3-\delta}$ composites [60]. The conductivity of the cermet with 40 vol% Ni was higher than that of the other compositions and decreased with increasing temperature (i.e., typical metallic conduction behavior). This indicates that the additional percolative electronic pathways in the Ni phase was absent in the cermets with lower (i.e., 30 vol% and 35 vol %) Ni contents. The hydrogen permeation flux through the cermet membranes containing 40 vol% Ni between 700°C and 800°C was 2.5 times higher than those of 35 vol% Ni, due to the increased electronic conduction contributed by the metallic Ni phase. The highest hydrogen permeation flux through a $230 \mu\text{m}$ -thick $\text{Ni-BaCe}_{0.9}\text{Y}_{0.1}\text{O}_{3-\delta}$ cermet membrane with 40 vol % Ni was $0.76 \text{ mL cm}^{-2} \text{ min}^{-1}$ at 800°C using a H_2 and He mixture and a H_2 and N_2 mixture in the feed and the sweep stream, respectively. A maximum flux of $0.805 \text{ mL cm}^{-2} \text{ min}^{-1}$ was obtained through a $266 \mu\text{m}$ -thick dense $\text{Ni-BaZr}_{0.1}\text{Ce}_{0.7}\text{Y}_{0.2}\text{O}_{3-\delta}$ cermet membrane with 40 vol% Ni at 900°C using 100% wet H_2 as feed gas and H_2/N_2 as sweep gas [62]. The hydrogen fluxes under wet conditions were higher than those under dry condition by a factor of four and three, at 600°C and 900°C , respectively. Given the very low possibility for the moisture to influence the hydrogen transport through the metal phase, it is most likely that the presence of moisture increased the proton conductivity in the ceramic phase, which subsequently led to the enhanced hydrogen flux of the dense $\text{Ni-BaZr}_{0.1}\text{Ce}_{0.7}\text{Y}_{0.2}\text{O}_{3-\delta}$ cermet membrane, relative to that in the dry condition. Since the electronic conductivity of nickel phase decreased with temperature rise, the hydrogen flux was

limited by the proton transport through the ceramic phase under wet condition. The $\text{Ni-Ba}_{0.8}\text{Ce}_{0.35}\text{Zr}_{0.5}\text{Tb}_{0.15}\text{O}_{3-\delta}$ cermet membrane with 40 vol% Ni was obtained by co-sintering NiO and $\text{Ba}_{0.8}\text{Ce}_{0.35}\text{Zr}_{0.5}\text{Tb}_{0.15}\text{O}_{3-\delta}$ powder mixture at 1550°C in reducing atmosphere [69]. The resultant field emission scanning electron microscopy (FESEM) image, elemental mapping, and energy dispersive X-ray diffraction (EDX) profile confirmed the presence of randomly distributed metallic nickel in the $\text{Ba}_{0.8}\text{Ce}_{0.35}\text{Zr}_{0.5}\text{Tb}_{0.15}\text{O}_{3-\delta}$ matrix (Fig. 6). $\text{Ni-Ba}_{0.8}\text{Ce}_{0.35}\text{Zr}_{0.5}\text{Tb}_{0.15}\text{O}_{3-\delta}$ membrane showed an electrical conductivity of $\sim 14 \text{ S cm}^{-1}$ at 700°C , which reduced further with temperature increase beyond 700°C . The 1.5 mm-thick cermet membrane showed a hydrogen permeation flux of $0.07 \text{ mL cm}^{-2} \text{ min}^{-1}$ at 900°C . The membrane also had good structural stability without any significant change in the hydrogen permeation flux performance.

Copper is another attractive alternative metal especially in carbon-containing atmospheres (relative to nickel). Rosesteel and Sullivan prepared a dense $\text{Cu-BaZr}_{0.9}\text{Y}_{0.1}\text{O}_{3-\delta}$ cermet membrane using a novel molten-copper infiltration method [68]. They did not co-sinter the proton-conducting ceramic and metal, unlike the previously discussed Ni-based cermet membranes cases. A hydrogen permeation flux of $4.6 \times 10^{-4} \text{ mL cm}^{-2} \text{ min}^{-1}$ was measured through a 1.90 mm-thick $\text{Cu-BaZr}_{0.9}\text{Y}_{0.1}\text{O}_{3-\delta}$ dense membrane with 60 vol% Cu at 882°C using 100% dry H_2 as feed gas and Ar as sweep gas. This is substantially lower than the hydrogen fluxes observed in the Ni-based cermet membranes. Such low hydrogen flux was attributed to the low fraction of $\text{BaZr}_{0.9}\text{Y}_{0.1}\text{O}_{3-\delta}$ phase ($\sim 74 \text{ wt\%}$ and $\sim 40 \text{ vol\%}$), the high tortuosity and the low protonic conductivity of the $\text{BaZr}_{0.9}\text{Y}_{0.1}\text{O}_{3-\delta}$ phase, and/or the interfacial resistance between $\text{BaZr}_{0.9}\text{Y}_{0.1}\text{O}_{3-\delta}$ and Cu phases [68]. The performance degradation of the $\text{Cu-BaZr}_{0.9}\text{Y}_{0.1}\text{O}_{3-\delta}$ membrane was evaluated periodically at 882°C , during which the membrane remained leak-free for over 30 days of testing (Fig. 7).

Membranes based on the third combination, at present, typically showed moderate hydrogen fluxes since the full potential of the interface between the proton conducting

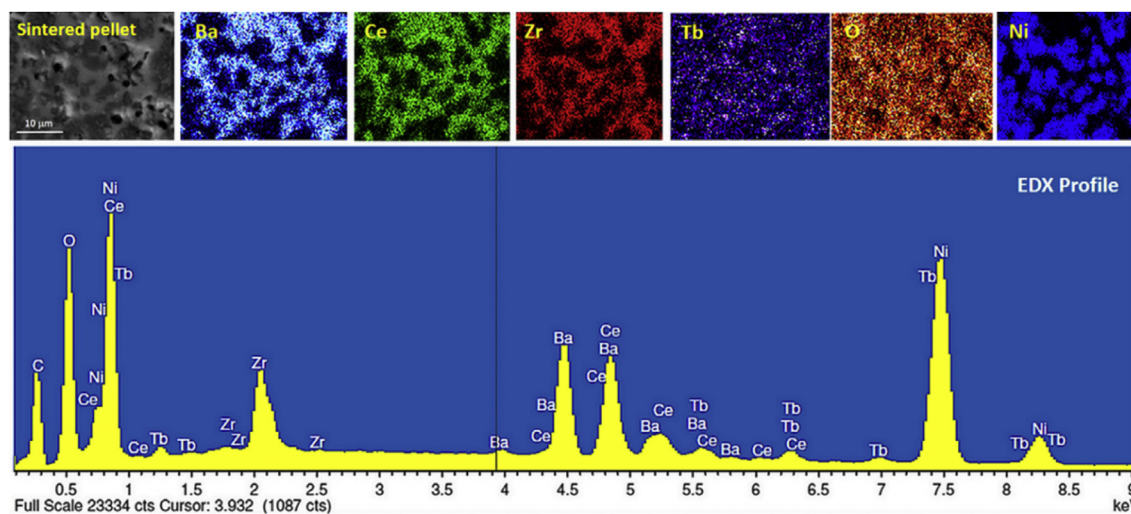


Fig. 6 – Field emission scanning electron microscopy surface morphology, elemental mapping, and energy dispersive X-ray diffraction profile of the $\text{Ni-Ba}_{0.8}\text{Ce}_{0.35}\text{Zr}_{0.5}\text{Tb}_{0.15}\text{O}_{3-\delta}$ membrane (Reproduced from [69]).

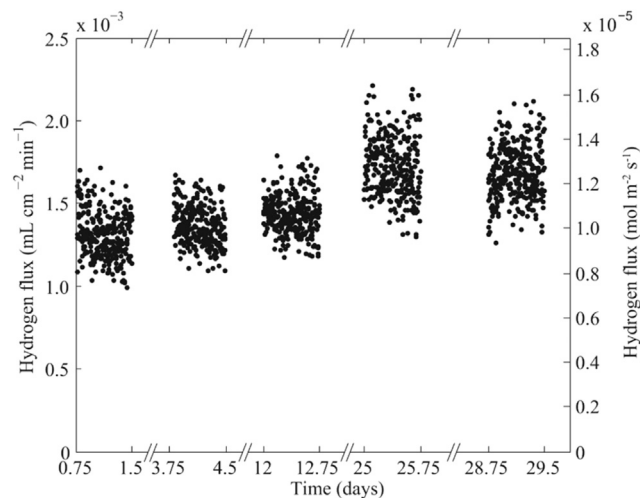


Fig. 7 – Hydrogen permeation of a 1.90 mm-thick Cu–BaZr_{0.9}Y_{0.1}O_{3-δ} dense membrane with 60 vol% Cu at the baseline condition of 882 °C under dry condition at a hydrogen partial pressure gradient of 0.5 bar with H₂ as feed gas and dry Ar as sweep gas during test for 30 days (Reproduced from [68]).

ceramic and the metal phases have not yet been accomplished [57]. Such interfacial features should be optimized to enhance the hydrogen permeation fluxes via optimizing the ambipolar diffusion. In most cases, the hydrogen transport through the cermet membranes occurs via the atomic diffusion through the metallic phase and not via the ambipolar diffusion. This limited ambipolar diffusion rate through the cermet membrane is closely associated to the non-optimized microstructure of the composite [60]. Sintering at high temperatures is normally required given the highly refractory nature of proton-conducting ceramics. Very high sintering temperatures, in most cases, lead to the agglomeration, loss, and segregation of the metallic phase [70]. Moreover, if the melting point of the metallic phase is substantially lower than the ceramic phase and the sintering rate is very slow, metallic phase can diffuse out before bonding with the ceramic matrix. Therefore, optimum sintering process is required to ensure that the co-sintering of the metallic and ceramic phases takes place without metal losses. Although Ni is cheaper than Pd, Ni may form volatile liquid phase

during high temperature sintering [71]. This leads to the possible reactions between the supposedly preserved individual phases [72]. The sintering of Ni-containing cermet membranes should be performed in inert atmosphere to avoid Ni oxidation to NiO [73].

Conceptually, apart from their high proton conductivities, perovskite-based proton conducting material can also exhibit electronic conductivity when transition metal cations occupy its B-site crystal lattice position. Its electronic conductivity however is generally lower than its ionic conductivity. In this case, its electronic conductivity can be enhanced further by adding a second electronically conducting polycrystalline ceramic phase. The two polycrystalline ceramic phases nonetheless should form the cermet composite with a certain degree of percolation for the continuous proton and electron transport pathways to be present across the membrane. Since these two phases are subjected to high temperature and reducing environments, these two phases should be chemically and thermally compatible to each other. Table 6 summarizes hydrogen permeation performances of several cermet membranes [72,74–77]. The addition of ZnO as the second phase was reported to improve the hydrogen flux performance of SrCe_{0.95}Y_{0.05}O_{3-δ} membrane [72]. A hydrogen flux of 0.039 mL cm⁻² min⁻¹ was measured at 900 °C for a 1.09 mm-thick SrCe_{0.95}Y_{0.05}O_{3-δ}-ZnO membrane with 10 vol% ZnO. Not only acting as the sintering aid, ZnO also contributed to enhance the electronic conductivity since it is an n-type electronic conductor under hydrogen containing atmosphere [78]. Moreover, its thermal expansion coefficient of $8 \times 10^{-6} \text{ K}^{-1}$ that is close to that of SrCeO₃ (i.e., $10.8 \times 10^{-6} \text{ K}^{-1}$) ensures minimized thermo-mechanical incompatibility between the two ceramic phases [79]. Fish et al. reported that the hydrogen permeation fluxes through a 1 mm-thick BaCe_{0.2}Zr_{0.7}Y_{0.1}O_{3-δ}-Sr_{0.95}Ti_{0.9}Nb_{0.1}O_{3-δ} membrane with 50 vol% Sr_{0.95}Ti_{0.9}Nb_{0.1}O_{3-δ} were as low as 2.4×10^{-7} – $4.8 \times 10^{-7} \text{ mL cm}^{-2} \text{ min}^{-1}$ at 900 °C [74]. These fluxes are comparable to those reported for single-phase membranes such as Eu- and Sm-doped SrCeO₃ [43]. However, these fluxes are still lower compared to the fluxes of cermet membranes such as Ni–BaCe_{0.9}Y_{0.1}O_{3-δ} and Pd–BaCe_{0.4}Zr_{0.4}Gd_{0.1}Dy_{0.1}O_{3-δ} [60,67]. A dual-phase BaCe_{0.8}Y_{0.2}O_{3-δ}-Ce_{0.8}Y_{0.2}O_{2-δ} membrane with 50 wt% BaCe_{0.8}Y_{0.2}O_{3-δ} was fabricated with a one-step simultaneous synthesis and sintering [75]. NiO was used to facilitate the phase formation and sintering. A hydrogen flux of 0.0107 mL cm⁻² min⁻¹ was attained at 900 °C for a

Table 6 – Dual-phase cermet proton conducting perovskite membranes performance overview for H₂ permeation [72,74–77].

Materials	H ₂ flux (mL cm ⁻² min ⁻¹)	Feed/sweep atmospheres	Temperature (°C)	Thickness (mm)	Note	Ref.
BaCe _{0.20} Zr _{0.70} Y _{0.10} O _{3-δ} -Sr _{0.95} Ti _{0.90} Nb _{0.10} O _{3-δ} (50:50 vol%)	1.07×10^{-2}	Dry 4% H ₂ + 96% He/Dry Ar	800	1	Disk	[74]
BaCe _{0.80} Zr _{0.20} O _{3-δ} -Ce _{0.80} Y _{0.20} O _{2-δ} (50:50 wt%)	7.44×10^{-2}	Wet 50% H ₂ + He + Ar/Ar	900	1.44	Disk	[75]
BaCe _{0.65} Zr _{0.20} Y _{0.15} O _{3-δ} -Ce _{0.85} Gd _{0.15} O _{2-δ} (50:50 vol%)	0.27	Wet 50% H ₂ + 50% He/Wet Ar	755	0.65	Disk	[76]
BaCe _{0.65} Zr _{0.20} Y _{0.15} O _{3-δ} -Ce _{0.85} Gd _{0.15} O _{2-δ} (50:50 vol%)	2.40	Dry 50% H ₂ + 50% He/Wet Ar	1040	0.65	Disk	[76]
BaCe _{0.65} Zr _{0.20} Y _{0.15} O _{3-δ} -Ce _{0.85} Gd _{0.15} O _{2-δ} (60:40 vol%)	0.14	Wet 50% H ₂ + 50% He/Wet Ar	755	0.66	Disk	[76]
BaCe _{0.65} Zr _{0.20} Y _{0.15} O _{3-δ} -Ce _{0.85} Y _{0.15} O _{2-δ} (50:50 vol%)	0.12	Wet 50% H ₂ + 50% He/Wet Ar	735	0.61	Disk	[76]
SrCe _{0.95} Y _{0.05} O _{3-δ} -ZnO (90:10 wt%)	3.90×10^{-2}	21% H ₂ + 79% He/N ₂	900	1.09	Disk	[72]
La _{5.5} WO _{11.25-δ} -La _{0.87} Sr _{0.13} CrO _{3-δ} (50:50 vol%)	0.15	Wet 50% H ₂ + 50% He/Wet Ar	700	0.37	Disk	[77]

1.44 mm-thick membrane. The hydrogen flux nevertheless degraded over time due to the formation of dopant deficient phase (i.e., Y) on the membrane feed side surface, which creates an increased inter-granular contact resistance. The presence of Ni particles inside the internal pores and at the grain boundaries can be ascribed to the NiO reduction to Ni during the permeation test. These metal particles increase the mechanical stresses between the grains, causing fracture in the $\text{BaCe}_{0.8}\text{Y}_{0.2}\text{O}_{3-\delta}$ - $\text{Ce}_{0.8}\text{Y}_{0.2}\text{O}_{2-\delta}$ membrane [75].

Escalárico et al. overcame the low electronic conductivity limitation of $\text{La}_{5.5}\text{WO}_{11.25-\delta}$ and the low sinterability of $\text{La}_{0.87}\text{Sr}_{0.13}\text{CrO}_{3-\delta}$ by preparing $\text{La}_{5.5}\text{WO}_{11.25-\delta}$ - $\text{La}_{0.87}\text{Sr}_{0.13}\text{CrO}_{3-\delta}$ dual-phase composites [77]. A maximum hydrogen flux of $0.15 \text{ mL cm}^{-2} \text{ min}^{-1}$ was obtained for a $370 \text{ }\mu\text{m}$ -thick $\text{La}_{5.5}\text{WO}_{11.25-\delta}$ - $\text{La}_{0.87}\text{Sr}_{0.13}\text{CrO}_{3-\delta}$ membrane with 50 vol% of $\text{La}_{5.5}\text{WO}_{11.25-\delta}$ at 700°C using wet H_2 in He as feed gas and Ar as sweep gas. The hydrogen permeation fluxes of the dual-phase membranes increased with increasing LWO content of up to 50 vol% given the increase in ambipolar conductivity. Rebollo et al. prepared a dual-phase membrane consisting of $\text{BaCe}_{0.65}\text{Zr}_{0.2}\text{Y}_{0.15}\text{O}_{3-\delta}$ and $\text{Ce}_{0.85}\text{Gd}_{0.15}\text{O}_{2-\delta}$ by mixing $\text{BaCe}_{0.65}\text{Zr}_{0.2}\text{Y}_{0.15}\text{O}_{3-\delta}$ and $\text{Ce}_{0.85}\text{Gd}_{0.15}\text{O}_{2-\delta}$ powders with ZnO as sintering aid via ball-milling for 1 h followed by drying and sieving [76]. The dried and sieved powders were then pressed and sintered, resulting in a 1-mm thick disks. The dual-phase $\text{BaCe}_{0.65}\text{Zr}_{0.2}\text{Y}_{0.15}\text{O}_{3-\delta}$ - $\text{Ce}_{0.85}\text{Gd}_{0.15}\text{O}_{2-\delta}$ membrane with 50 vol% of $\text{Ce}_{0.85}\text{Gd}_{0.15}\text{O}_{2-\delta}$ was chosen because of its higher hydrogen flux and better stability under dry and wet permeation conditions compared to the membrane with 40 vol% $\text{Ce}_{0.85}\text{Gd}_{0.15}\text{O}_{2-\delta}$ content. Four hydration conditions were utilized to determine the predominant transport mechanism in the $\text{BaCe}_{0.65}\text{Zr}_{0.2}\text{Y}_{0.15}\text{O}_{3-\delta}$ - $\text{Ce}_{0.85}\text{Gd}_{0.15}\text{O}_{2-\delta}$ membrane, i.e., (C1) both feed and permeate sides are dry; (C2) only the feed side is humidified; (C3) both feed and permeate sides are humidified; and (C4) only the permeate side is humidified. The experiments under C1 conditions were not successful due to the mechanical failure under reducing conditions and the gold sealing failure at high temperatures. Fig. 8(a) shows that the hydrogen permeation flux was very low when only the feed side was humidified (C2) because of the insufficient protonic charge carriers. Furthermore, an increase in the hydrogen

permeation flux can be observed when both feed and permeate sides were humidified (C3). This is attributed to the contribution of the hydrogen permeation through the membrane and the hydrogen production via water splitting. Further increase in the hydrogen permeation flux was obtained under C4 condition given the increase in the oxygen ion transport through the membrane caused by the higher oxygen partial pressure gradient between the feed side and permeate side. A sharp increase in the hydrogen permeation flux variation obtained by the step-change from C3 to C4 conditions at 750°C reflects the effect of water splitting on the hydrogen production (Fig. 8(b)). In addition, Fig. 8(c) shows increase of hydrogen permeation fluxes with increasing temperature and hydrogen partial pressure. Increasing hydrogen fluxes up to $1.75 \text{ mL cm}^{-2} \text{ min}^{-1}$ and $2.40 \text{ mL cm}^{-2} \text{ min}^{-1}$ at 1040°C were observed when both membrane sides and only the sweep side were hydrated, respectively.

Asymmetric membranes

As the membrane becomes sufficiently thin, proton diffusion across the membrane no longer becomes the rate limiting step for the overall hydrogen flux. Surface reaction play a more essential role to further increase the hydrogen flux of very thin membrane; the rate of which depends on the concentration of triple phase boundaries, i.e., the interfaces between the proton conducting phase, the electron conducting phase, and the gas phase. An asymmetric structure combines a porous substrate with a thin dense layer to overcome the thickness limitation (i.e., due to relatively high thickness of the disk membrane) without compromising the mechanical integrity. The porous layer provides the mechanical strength while allowing gas transport through its porous channels. Its thermal expansion nonetheless should match that of the thin dense layer to prevent structure cracking during sintering. Similar material is usually used for both porous and dense layers to avoid thermal expansion mismatch between these two layers. Adequate gas diffusion flow to supply hydrogen gas to the dense layer should also be ensured in choosing suitable porous substrate. The dense layer can be fabricated

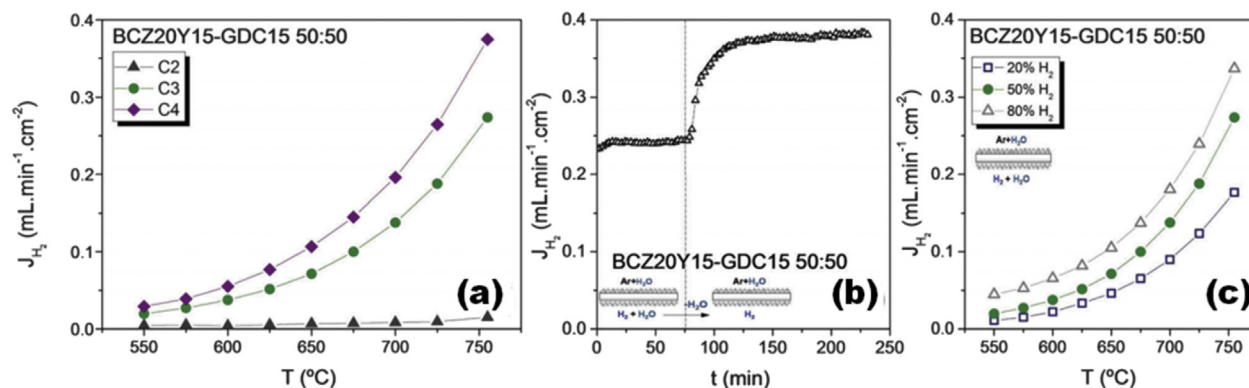


Fig. 8 – (a) Hydrogen permeation flux as a function of temperature for a $650\text{-}\mu\text{m}$ thick $\text{BaCe}_{0.65}\text{Zr}_{0.2}\text{Y}_{0.15}\text{O}_{3-\delta}$ - $\text{Ce}_{0.85}\text{Gd}_{0.15}\text{O}_{2-\delta}$ membrane measured in three different configurations (C2, C3, and C4) with a mixture of 50 vol% H_2 in He as the feed gas; (b) Hydrogen permeation flux variation when hydration configuration changes from C3 to C4 at 755°C with a mixture of 50 vol% H_2 in He as the feed gas; and (c) H_2 flux as a function of temperature under C3 conditions with different hydrogen partial pressures in the feed (Reproduced from [76]).

Table 7 – Asymmetric proton conducting perovskite membranes performance overview for H₂ permeation [38,80–87].

Materials	H ₂ flux (mL cm ⁻² min ⁻¹)	Feed/sweep atmospheres	Temperature (°C)	Thickness (mm)	Note	Ref.
SrCe _{0.95} Tm _{0.05} O _{3-δ}	0.125	10% H ₂ + 90% He/Air	900	0.15	Asymmetric disk Substrate: Porous SrCe _{0.95} Tm _{0.05} O _{3-δ} Citrate method Dry pressing	[38]
SrCe _{0.95} Yb _{0.05} O _{3-δ}	0.013	H ₂ + He (or N ₂)/N ₂ + O ₂ + He	677	0.002	Asymmetric disk Substrate: Porous SrZr _{0.95} Y _{0.05} O _{3-δ} Combustion method Spin coating	[82]
SrCe _{0.7} Zr _{0.2} Eu _{0.1} O _{3-δ}	0.23	100% H ₂ /He	900	0.033	Tubular support: NiO– SrCe _{0.8} Zr _{0.2} O _{3-δ} Thin film: SrCe _{0.7} Zr _{0.2} Eu _{0.1} O _{3-δ} Solid state reaction Support: Tape casting and rolling Thin film: Slurry coating	[83]
SrCe _{0.7} Zr _{0.2} Eu _{0.1} O _{3-δ}	0.21	97% H ₂ + 3% H ₂ O/He	900	0.033	Tubular support: NiO– SrCe _{0.8} Zr _{0.2} O _{3-δ} Thin film: SrCe _{0.7} Zr _{0.2} Eu _{0.1} O _{3-δ} Solid state reaction Support: Tape casting and rolling Thin film: Slurry coating	[83]
Sr(Ce _{0.6} Zr _{0.4}) _{0.85} Y _{0.15} O _{3-δ}	1.84 × 10 ⁻⁴	H ₂ /Ar	800	0.017	Asymmetric disk Substrate: Porous Sr(Ce _{0.6} Zr _{0.4}) _{0.85} Y _{0.15} O _{3-δ} Film: 10 layers of NiO/SCZY tape and one layer of SCZY Sol-gel Tape casting and co-pressing	[84]
BaCe _{0.90} Y _{0.10} O _{3-δ}	0.113	Dry 10% H ₂ + 90% N ₂ /Ar	800	0.01	Asymmetric disk Substrate: Porous ZrO ₂	[80]
BaCe _{0.90} Y _{0.10} O _{3-δ} - rapidly solidified Zr (RSZ)	0.17	Dry 10% H ₂ + 90% N ₂ /Ar	800	0.01	Asymmetric disk Substrate: Porous ZrO ₂	[80]
BaCe _{0.85} Tb _{0.05} Zr _{0.1} O _{3-δ}	0.07 (Stable over 370 h)	50% H ₂ + 50% He/Ar	800	0.05	Asymmetric disk Substrate: Porous BaCe _{0.85} Tb _{0.05} Zr _{0.1} O _{3-δ} Glycine nitrate combustion Co-pressing and co-sintering Substrate: Porous BaCe _{0.85} Tb _{0.05} Zr _{0.1} O _{3-δ}	[81]
Ni–BaCe _{0.95} Tb _{0.05} O _{3-δ} (50:50 wt%)	0.914	50% H ₂ + 50% N ₂ /He	850	0.09	Asymmetric disk Substrate: Porous Ni–BaCe _{0.95} Tb _{0.05} O _{3-δ}	[85]
Ni–BaZr _{0.10} Ce _{0.70} Y _{0.20} O _{3-δ} (55:45 wt%)	0.32	80% H ₂ + 17% He + 3% H ₂ O/Dry Ar	900	0.003	Asymmetric disk Substrate: Porous Ni–BaCe _{0.70} Zr _{0.10} Y _{0.20} O _{3-δ}	[86]
Ni–BaZr _{0.10} Ce _{0.70} Y _{0.10} Yb _{0.10} O _{3-δ} (40:60 vol%)	0.49	Dry 100% H ₂ /He	700	0.044	Asymmetric disk Substrate: Porous Ni–BaZr _{0.10} Ce _{0.70} Y _{0.10} Yb _{0.10} O _{3-δ}	[87]
Ni–BaZr _{0.10} Ce _{0.70} Y _{0.10} Yb _{0.10} O _{3-δ} (40:60 vol%)	1.12	Dry 100% H ₂ /He	900	0.044	Asymmetric disk Substrate: Porous Ni–BaZr _{0.10} Ce _{0.70} Y _{0.10} Yb _{0.10} O _{3-δ}	[87]

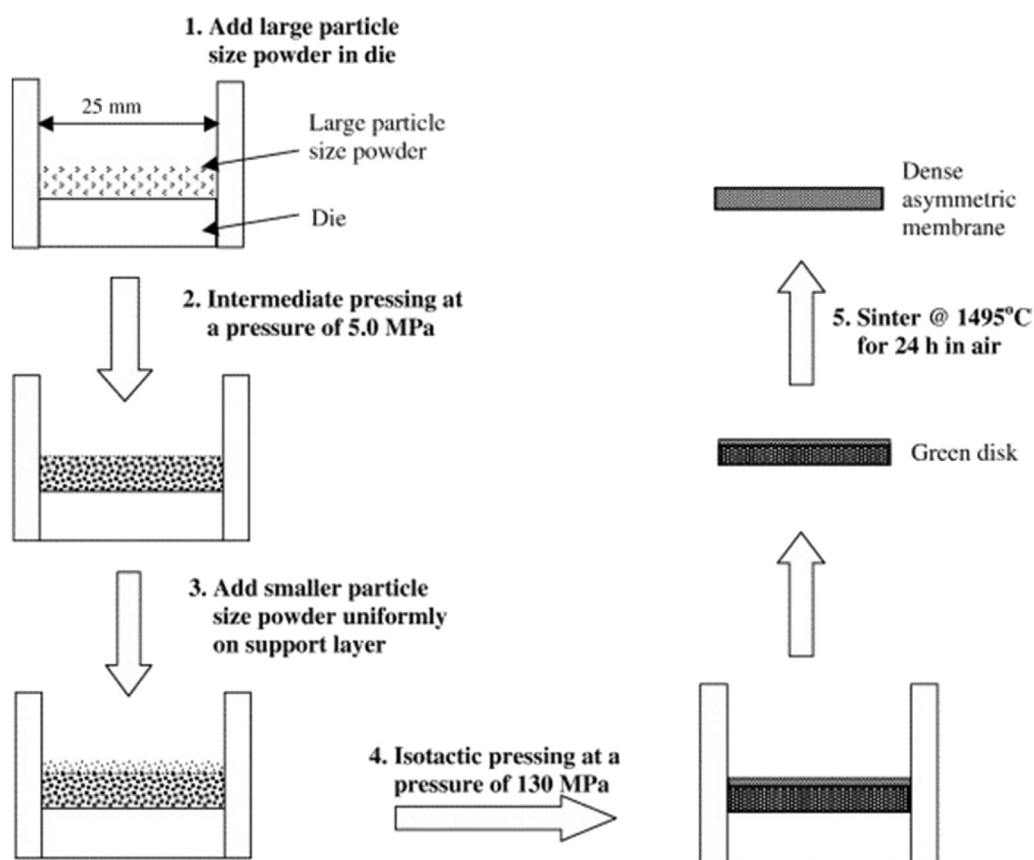


Fig. 9 – Illustration of dry pressing procedure to make a disk-shaped $\text{SrCe}_{0.95}\text{Tm}_{0.05}\text{O}_{3-\delta}$ asymmetrical membrane (Reproduced from [38]).

using various methods such as spin coating, sputtering, e-beam evaporation, metal organic chemical vapor, and aerosol deposition. Hydrogen permeation performances of several asymmetric disk membranes are summarized in Table 7 [38,80–87].

A simple technique such as dry-pressing method can be utilized to fabricate two-layer asymmetric disk membrane consisting of dense layer of $\text{SrCe}_{0.95}\text{Tm}_{0.05}\text{O}_{3-\delta}$ on top of a porous disk of similar material [38]. Both dense and porous layers forming the asymmetric $\text{SrCe}_{0.95}\text{Tm}_{0.05}\text{O}_{3-\delta}$ membranes were obtained by controlling the particle size of powders while the thickness of the dense layer was controlled by varying the amount of powders used. Fig. 9 shows the schematic illustration of the dry pressing process to make asymmetric disks [38]. An initially low pressure of 5 MPa was applied to facilitate a porous $\text{SrCe}_{0.95}\text{Tm}_{0.05}\text{O}_{3-\delta}$ layer formation followed by the addition of smaller particle size powder uniformly on the support layer before the sample was pressed again at a higher pressure of 130 MPa. The amount of powder was varied from 0.2 g to 2 g to vary the thickness of the dense top layer. For each $\text{SrCe}_{0.95}\text{Tm}_{0.05}\text{O}_{3-\delta}$ membrane, the total powder amount used was 4.2 g. The green disks were finally sintered in air at 1495 °C for 24 h. A maximum hydrogen flux of $0.13 \text{ mL cm}^{-2} \text{ min}^{-1}$ was obtained at 900 °C for a 150 μm -thick membrane using 10 vol% H_2 in He as feed and air as sweep gas, which is four times higher than the symmetric 1.6 mm-thick $\text{SrCe}_{0.95}\text{Tm}_{0.05}\text{O}_{3-\delta}$ membrane.

Kim et al. utilized an aerosol deposition method to form a 0.01 mm-thick dense layer of $\text{BaCe}_{0.90}\text{Y}_{0.10}\text{O}_{3-\delta}$ and $\text{BaCe}_{0.90}\text{Y}_{0.10}\text{O}_{3-\delta}$ -rapidly solidified Zr (RSZ) on top of a 2 mm-thick porous disk of ZrO_2 [80]. Their method involves the fabrication of thin films at room temperature without any phase change. The resultant hydrogen permeation fluxes at 800 °C under dry hydrogen ambient for the $\text{BaCe}_{0.90}\text{Y}_{0.10}\text{O}_{3-\delta}$ and $\text{BaCe}_{0.90}\text{Y}_{0.10}\text{O}_{3-\delta}$ -RSZ composite membranes were $0.113 \text{ mL cm}^{-2} \text{ min}^{-1}$ and $0.17 \text{ mL cm}^{-2} \text{ min}^{-1}$, respectively. Moreover, the higher hydrogen permeability of $\text{BaCe}_{0.90}\text{Y}_{0.10}\text{O}_{3-\delta}$ -RSZ composite membrane can be attributed to its higher electrocatalytic activity due to the addition of melt-spun Zr-based alloy. The presence of Ba–Ce oxide alloy that suppresses the embrittlement also contributed to the improved flux performance. The hydrogen permeation flux through a 50 μm -thick dense $\text{BaCe}_{0.85}\text{Tb}_{0.05}\text{Zr}_{0.1}\text{O}_{3-\delta}$ asymmetric membrane prepared using dry-pressing method was stable at $0.07 \text{ mL cm}^{-2} \text{ min}^{-1}$ for over 370 h at 800 °C [81]. No flux reduction was observed with increasing time using 50 vol% H_2 and 50 vol% He as feed gas. Moreover, X-ray diffraction showed that both $\text{BaCe}_{0.85}\text{Tb}_{0.05}\text{Zr}_{0.1}\text{O}_{3-\delta}$ asymmetric membrane surfaces sustain their perovskite structure indicating the good phase structure stability of $\text{BaCe}_{0.85}\text{Tb}_{0.05}\text{Zr}_{0.1}\text{O}_{3-\delta}$ after long-term hydrogen permeation test under reducing atmospheres.

Hamakawa et al. deposited $\text{SrCe}_{0.95}\text{Yb}_{0.05}\text{O}_{3-\delta}$ thin film on porous $\text{SrZr}_{0.95}\text{Y}_{0.05}\text{O}_{3-\delta}$ substrate [82]. $\text{SrZr}_{0.95}\text{Y}_{0.05}\text{O}_{3-\delta}$ was chosen as the porous substrate material due to its higher

mechanical strength compared to $\text{SrCe}_{0.95}\text{Yb}_{0.05}\text{O}_{3-\delta}$. The precursor powders were prepared by combustion method while the porous $\text{SrZr}_{0.95}\text{Y}_{0.05}\text{O}_{3-\delta}$ disk-shaped substrates were fabricated by uniaxial pressing at 120 MPa. To vary the film thickness, the spin coating–drying–sintering cycles were repeated several times (i.e., $\sim 2\text{ }\mu\text{m}$ -thick film was deposited during each cycle). The hydrogen permeation flux of a $2\text{ }\mu\text{m}$ -thick dense film was 500 times greater than that of the 1-mm $\text{SrCe}_{0.95}\text{Yb}_{0.05}\text{O}_{3-\delta}$ symmetric membrane disk. The thickness-dependent hydrogen permeation fluxes data for the asymmetric $\text{SrCe}_{0.95}\text{Yb}_{0.05}\text{O}_{3-\delta}$ membrane at $677\text{ }^{\circ}\text{C}$ and hydrogen feed partial pressure of 20 kPa indicates the dominance of bulk-diffusion step down to $2\text{-}\mu\text{m}$ -thick film (the thinnest membrane tested) at such relatively low temperature (Fig. 10). The synthesis procedure adopted by Hamakawa et al. [82] is however, arduous and requires delicate approach, which is impractical for large-scale application.

A maximum hydrogen permeation flux of $0.23\text{ mL cm}^{-2}\text{ min}^{-1}$ and $0.21\text{ mL cm}^{-2}\text{ min}^{-1}$ was obtained at $900\text{ }^{\circ}\text{C}$ using 100 vol% H_2 and 3 vol% H_2O in H_2 as feed gas, respectively, for a $33\text{ }\mu\text{m}$ -thick dense $\text{SrCe}_{0.7}\text{Zr}_{0.2}\text{Eu}_{0.1}\text{O}_{3-\delta}$ supported on a porous $\text{Ni-SrCe}_{0.8}\text{Zr}_{0.2}\text{O}_{3-\delta}$ tubular substrate [83]. The tubular substrate was fabricated by tape-casting and rolling techniques while the pores on the porous $\text{Ni-SrCe}_{0.8}\text{Zr}_{0.2}\text{O}_{3-\delta}$ were formed via NiO reduction to Ni . Eu was not introduced as a component to the substrate composition since it was not necessary for the membrane support to be electronically conductive. $\text{SrCe}_{0.7}\text{Zr}_{0.2}\text{Eu}_{0.1}\text{O}_{3-\delta}$ was coated on the inner side of the pre-sintered support by colloidal coating before finally sintered at $1520\text{ }^{\circ}\text{C}$ in air. The preparation of thin supported $\text{SrCe}_{0.7}\text{Zr}_{0.2}\text{Eu}_{0.1}\text{O}_{3-\delta}$ membranes has been discussed in more detail by Yoon et al. [88].

The tape casting method has also been applied to fabricate an asymmetric $\text{Sr}(\text{Ce}_{0.6}\text{Zr}_{0.4})_{0.85}\text{Y}_{0.15}\text{O}_{3-\delta}$ membrane [84]. Ten

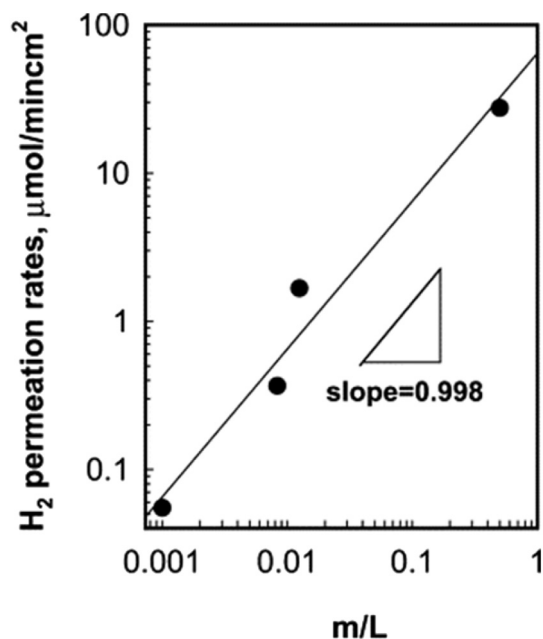


Fig. 10 – Thickness-dependent hydrogen permeation flux of $\text{SrCe}_{0.95}\text{Yb}_{0.05}\text{O}_{3-\delta}$ thin film at $677\text{ }^{\circ}\text{C}$ and hydrogen feed partial pressure of 20 kPa (Reproduced from [82]).

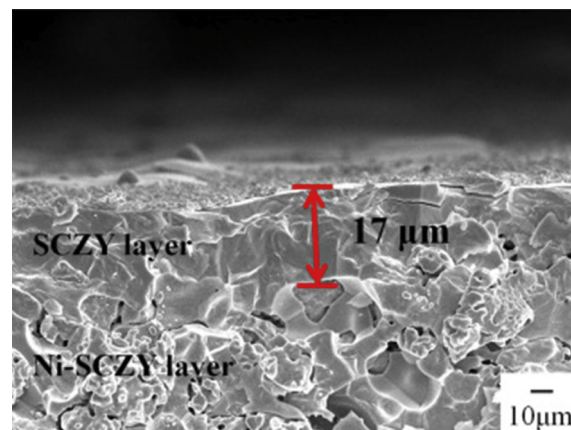


Fig. 11 – The cross-sectional scanning electron microscopy image of $\text{Sr}(\text{Ce}_{0.6}\text{Zr}_{0.4})_{0.85}\text{Y}_{0.15}\text{O}_{3-\delta}/\text{Ni-Sr}(\text{Ce}_{0.6}\text{Zr}_{0.4})_{0.85}\text{Y}_{0.15}\text{O}_{3-\delta}$ membrane (Reproduced from [84]).

layers of $\text{NiO}/\text{Sr}(\text{Ce}_{0.6}\text{Zr}_{0.4})_{0.85}\text{Y}_{0.15}\text{O}_{3-\delta}$ tape and one layer of $\text{Sr}(\text{Ce}_{0.6}\text{Zr}_{0.4})_{0.85}\text{Y}_{0.15}\text{O}_{3-\delta}$ tape were pressed at 90 MPa followed by sintering at $1450\text{ }^{\circ}\text{C}$ for 2 h. Fig. 11 shows the cross-sectional SEM micrograph of the $\text{Sr}(\text{Ce}_{0.6}\text{Zr}_{0.4})_{0.85}\text{Y}_{0.15}\text{O}_{3-\delta}/\text{Ni-Sr}(\text{Ce}_{0.6}\text{Zr}_{0.4})_{0.85}\text{Y}_{0.15}\text{O}_{3-\delta}$ membrane. A $17\text{ }\mu\text{m}$ -thick dense $\text{Sr}(\text{Ce}_{0.6}\text{Zr}_{0.4})_{0.85}\text{Y}_{0.15}\text{O}_{3-\delta}$ membrane is well-attached to the $\text{Ni-Sr}(\text{Ce}_{0.6}\text{Zr}_{0.4})_{0.85}\text{Y}_{0.15}\text{O}_{3-\delta}$ porous substrate. Note that the pores on the porous $\text{Ni-Sr}(\text{Ce}_{0.6}\text{Zr}_{0.4})_{0.85}\text{Y}_{0.15}\text{O}_{3-\delta}$ substrate formed when the carbon powder (i.e., pore former) was oxidized into gas products and NiO is reduced to Ni . A maximum hydrogen permeation flux of $4.12\text{ mL cm}^{-2}\text{ min}^{-1}$ was obtained at $800\text{ }^{\circ}\text{C}$.

The asymmetric $\text{Ni-BaCe}_{0.95}\text{Tb}_{0.05}\text{O}_{3-\delta}$ cermet membrane containing $90\text{ }\mu\text{m}$ -thick dense layer on top of a porous disk of $\text{Ni-BaCe}_{0.95}\text{Tb}_{0.05}\text{O}_{3-\delta}$ was fabricated using the dry-pressing method [85]. A pressure of 10 MPa was used to facilitate a dense layer formation followed by sintering at $1400\text{ }^{\circ}\text{C}$ in pure nitrogen atmosphere for 10 h. The hydrogen permeation fluxes were improved by two times relative to the 0.65 mm dense disk $\text{Ni-BaCe}_{0.95}\text{Tb}_{0.05}\text{O}_{3-\delta}$ membrane, reaching up to $0.914\text{ mL cm}^{-2}\text{ min}^{-1}$ at $850\text{ }^{\circ}\text{C}$ when using the 50% H_2/N_2 mixture feed and He as the sweep gas, respectively. The $\text{Ni-BaCe}_{0.95}\text{Tb}_{0.05}\text{O}_{3-\delta}$ cermet membranes however, were not stable under long-term hydrogen permeation test due to the phase decomposition of the $\text{BaCe}_{0.95}\text{Tb}_{0.05}\text{O}_{3-\delta}$ perovskite. Two-step sintering process was employed by Liu et al. [86] to prepare an asymmetric membrane consisting of 0.03 mm -thick dense $\text{Ni-BaCe}_{0.70}\text{Zr}_{0.10}\text{Y}_{0.20}\text{O}_{3-\delta}$ membrane layer and $\text{Ni-BaCe}_{0.70}\text{Zr}_{0.10}\text{Y}_{0.20}\text{O}_{3-\delta}$ porous substrate. For the porous substrate, a pore-forming agent (i.e., soluble starch) was added into the powder followed by compaction at 400 MPa and calcination in ambient air at $600\text{ }^{\circ}\text{C}$ for 3 h. The pre-sintered bi-layers were subsequently sintered at $1400\text{ }^{\circ}\text{C}$ for 10 h in 5 vol% H_2 and 95 vol% Ar to obtain dense top layer. A maximum hydrogen flux of $0.32\text{ mL cm}^{-2}\text{ min}^{-1}$ was observed at $900\text{ }^{\circ}\text{C}$ using 80 vol% H_2 in N_2 with 3 vol% of H_2O as feed and dry high purity argon as sweep gas. This flux is higher than that displayed by the symmetric $\text{Ni-BaCe}_{0.70}\text{Zr}_{0.10}\text{Y}_{0.20}\text{O}_{3-\delta}$ membranes [61,63].

A $44\text{ }\mu\text{m}$ -thick dense $\text{Ni-BaZr}_{0.1}\text{Ce}_{0.7}\text{Y}_{0.1}\text{Yb}_{0.1}\text{O}_{3-\delta}$ membrane supported on a porous $\text{Ni-BaZr}_{0.1}\text{Ce}_{0.7}\text{Y}_{0.1}\text{Yb}_{0.1}\text{O}_{3-\delta}$

substrate was fabricated using particle suspension coating process [87]. The $\text{NiO}-\text{BaZr}_{0.1}\text{Ce}_{0.7}\text{Y}_{0.1}\text{Yb}_{0.1}\text{O}_{3-\delta}$ suspension was prepared by dispersing the mixed $\text{NiO}-\text{BaZr}_{0.1}\text{Ce}_{0.7}\text{Y}_{0.1}\text{Yb}_{0.1}\text{O}_{3-\delta}$ powder in ethanol with a small amount of binder and dispersant. Using 100 vol% wet H_2 as feed gas and dry N_2 as sweep gas, the maximum hydrogen fluxes achieved were $0.49 \text{ mL cm}^{-2} \text{ min}^{-1}$ and $1.12 \text{ mL cm}^{-2} \text{ min}^{-1}$ at 700°C and 900°C , respectively. These considerably high fluxes suggest that the particle suspension coating resulted in improvement of the membrane-porous substrate interface, which increases the number of active sites for electrochemical reaction. Liu et al. reported that the hydrogen permeation through a $44 \mu\text{m}$ -thick asymmetric $\text{Ni}-\text{BaZr}_{0.1}\text{Ce}_{0.7}\text{Y}_{0.1}\text{Yb}_{0.1}\text{O}_{3-\delta}$ membrane was controlled by surface exchange reactions [87].

Hollow fiber membranes

Depending on the particular phase inversion process adopted, hollow fiber membrane with distinct asymmetric structure, i.e., thin dense layer made sandwiched by two porous layers or thin dense layer on top of the porous layer can be synthesized. The fact that these layers are made of the same material and are fabricated from single process eliminates the thermomechanical compatibility issue. Hollow fiber configuration provides advantages of very large surface area per unit volume and very thin transport layer (or very low transport resistance), which is very attractive for industrial application. At present, the major challenge lies in the mechanical strength of the hollow fiber which can be addressed by bundling the hollow fiber or using multi-bore design [89–91]. Hydrogen permeation performances of several hollow fiber membranes are summarized in Table 8 [48,92–98].

Li and co-workers prepared for the first time $\text{SrCe}_{0.95}\text{Yb}_{0.05}\text{O}_{3-\delta}$ hollow fiber membrane using an immersion induced phase inversion technique [99]. Following this work, they

performed another work on $\text{SrCe}_{0.95}\text{Yb}_{0.05}\text{O}_{3-\delta}$ with focus on sintering conditions [100]. They studied the effect of sintering temperature and time on the surface morphology, grain growth, and pore evolution or elimination to develop mechanically strong and gas-tight $\text{SrCe}_{0.95}\text{Yb}_{0.05}\text{O}_{3-\delta}$ hollow fiber membranes [100]. In another work, Li and co-workers evaluated the hydrogen permeation performance of $\text{SrCe}_{0.95}\text{Yb}_{0.05}\text{O}_{3-\delta}$ hollow fiber [92]. A maximum hydrogen flux of $0.2 \text{ mL cm}^{-2} \text{ min}^{-1}$ was observed at 950°C with the hydrogen concentration in the feed of 35.9%. Such low hydrogen flux was attributed to the densification of both inner and outer membrane surfaces that occurs during sintering, leading to the almost identical effective transport thickness for the hollow fiber and the fiber wall thickness. The hydrogen flux of the fiber can be improved if the inner or outer dense layer is eliminated [92].

Tan et al. showed that the hydrogen permeation flux performance of $\text{BaCe}_{0.8}\text{Yb}_{0.2}\text{O}_{3-\delta}$ disk membrane can be increased by adopting a hollow fiber configuration [48]. Sol-gel route was used to synthesize the $\text{BaCe}_{0.8}\text{Yb}_{0.2}\text{O}_{3-\delta}$ powder with 1 wt% Co_2O_3 was added into the prepared powder to improve the densification process during sintering. A gas-tight $\text{BaCe}_{0.8}\text{Yb}_{0.2}\text{O}_{3-\delta}$ hollow fiber membranes with improved mechanical strength was obtained at an optimum sintering temperature of 1400°C . The densification process to obtain the gas-tight $\text{BaCe}_{0.8}\text{Yb}_{0.2}\text{O}_{3-\delta}$ hollow fiber could not be achieved at the highest sintering temperature of 1550°C without the addition of Co_2O_3 . A hydrogen permeation flux of $0.38 \text{ mL cm}^{-2} \text{ min}^{-1}$ was obtained at 1050°C using 25% H_2 in He as feed gas on the shell side and N_2 as sweep gas in the fiber lumen, which is substantially higher compared to $0.01 \text{ mL cm}^{-2} \text{ min}^{-1}$ for 1 mm-thick $\text{BaCe}_{0.8}\text{Yb}_{0.2}\text{O}_{3-\delta}$ membrane disk.

Tan et al. investigated the hydrogen permeation flux performance of $\text{BaCe}_{0.95}\text{Tb}_{0.05}\text{O}_{3-\delta}$ hollow fiber membranes with an effective thickness of $100 \mu\text{m}$ [93]. A hydrogen flux of $0.57 \text{ mL cm}^{-2} \text{ min}^{-1}$ was obtained at 1000°C using 50% H_2 in He

Table 8 – Hollow fiber proton conducting perovskite membranes performance overview for H_2 permeation [48,92–98].

Materials	H_2 flux ($\text{mL cm}^{-2} \text{ min}^{-1}$)	Feed/sweep atmospheres	Temperature ($^\circ\text{C}$)	Thickness (mm)	Note	Ref.
$\text{SrCe}_{0.95}\text{Yb}_{0.05}\text{O}_{3-\delta}$	0.2	35.9% H_2 + 64.1% Ar/Dry air	950	–		[92]
$\text{BaCe}_{0.80}\text{Y}_{0.20}\text{O}_{3-\delta}$	0.38	50% H_2 + 50% He/ N_2	1050	0.20		[48]
$\text{BaCe}_{0.95}\text{Tb}_{0.05}\text{O}_{3-\delta}$	0.57	50% H_2 + 50% He/ N_2	1000	0.10		[93]
$\text{BaCe}_{0.85}\text{Tb}_{0.05}\text{Co}_{0.1}\text{O}_{3-\delta}$	0.385	50% H_2 + 50% He/ N_2	1000	0.163	Sol-gel method	[94]
$\text{BaCe}_{0.95}\text{Tb}_{0.05}\text{O}_{3-\delta}$ / $\text{NiO}-\text{BaCe}_{0.95}\text{Tb}_{0.05}\text{O}_{3-\delta}$	0.53	50% H_2 + 50% He/He	850	0.015	Combined phase inversion and sintering technique	[95]
$\text{BaCe}_{0.95}\text{Tb}_{0.05}\text{O}_{3-\delta}$	0.53	50% H_2 + 50% He/ N_2	850	0.015	$\text{BaCe}_{0.95}\text{Tb}_{0.05}\text{O}_{3-\delta}$ membrane coated on $\text{NiO}-$ $\text{BaCe}_{0.95}\text{Tb}_{0.05}\text{O}_{3-\delta}$ hollow fiber	[96]
$\text{BaCe}_{0.85}\text{Tb}_{0.05}\text{Co}_{0.1}\text{O}_{3-\delta}$	0.009	50% H_2 + 50% He/ N_2	700	OD: 1.70 ID: 1.08 Dense: 0.132	Porous $\text{NiO}-$ $\text{BaCe}_{0.95}\text{Tb}_{0.05}\text{O}_{3-\delta}$ -coated layer	[97]
$\text{BaCe}_{0.85}\text{Tb}_{0.05}\text{Co}_{0.1}\text{O}_{3-\delta}$	0.164	50% H_2 + 50% He/ N_2	1000	OD: 1.70 ID: 1.08 Dense: 0.132	Sol-gel method Combined phase inversion and sintering technique	[97]
$\text{BaCe}_{0.95}\text{Tb}_{0.05}\text{O}_{3-\delta}$	0.046	50% H_2 + 50% He/ N_2	900	0.10	Sol-gel method	[98]
$\text{BaCe}_{0.95}\text{Tb}_{0.05}\text{O}_{3-\delta}$	0.272	50% H_2 + 50% He/ N_2	900	0.10	Porous Pd-coated	[98]

as feed gas on the shell side and N_2 as sweep gas in the fiber lumen. Despite higher electrical conductivity due to Co-doping, the $BaCe_{0.85}Tb_{0.05}Co_{0.1}O_{3-\delta}$ hollow fiber membranes displayed lower hydrogen permeation fluxes [94] than the non-doped $BaCe_{0.95}Tb_{0.05}O_{3-\delta}$ hollow fiber membrane [93]. The maximum hydrogen permeation flux obtained at 1000 °C was only $0.385 \text{ mL cm}^{-2} \text{ min}^{-1}$ compared to $0.57 \text{ mL cm}^{-2} \text{ min}^{-1}$ for the non-doped $BaCe_{0.95}Tb_{0.05}O_{3-\delta}$ hollow fiber membrane. This decrease was attributed to a larger effective thickness of the $BaCe_{0.85}Tb_{0.05}Co_{0.1}O_{3-\delta}$ hollow fibers i.e., 163 μm compared to only 100 μm for the non-doped $BaCe_{0.95}Tb_{0.05}O_{3-\delta}$ hollow fibers. Moreover, a less developed porous layer on the inner surface side of the $BaCe_{0.85}Tb_{0.05}Co_{0.1}O_{3-\delta}$ hollow fibers led to a lower hydrogen permeation flux due to the slower surface exchange kinetics. Instead of limited by the electronic conductivity, the hydrogen permeation of the $BaCe_{0.85}Tb_{0.05}Co_{0.1}O_{3-\delta}$ membrane appears to be limited by the proton conductivity. This results in the limited hydrogen permeation flux of the $BaCe_{0.85}Tb_{0.05}Co_{0.1}O_{3-\delta}$ membrane. Song et al. suggested the optimization of the $BaCe_{0.85}Tb_{0.05}Co_{0.1}O_{3-\delta}$ hollow fiber microstructure to improve the hydrogen permeation flux [94].

Considering that the dense $Ni-BaZr_{0.1}Ce_{0.7}Y_{0.2}O_{3-\delta}$ cermet membranes provide high hydrogen permeation fluxes and chemical stability in CO_2 , H_2O , and H_2S -containing atmospheres, Yang et al. used this material for the preparation of hollow fiber membranes and studied their microstructure and hydrogen permeation performance [95]. One-step nitrate-citrate method was utilized to prepare the $NiO-BaZr_{0.1}Ce_{0.7}Y_{0.2}O_{3-\delta}$ composite powders followed by combined phase inversion and sintering in reduced atmosphere. Fig. 12 shows that the $Ni-BaZr_{0.1}Ce_{0.7}Y_{0.2}O_{3-\delta}$ hollow fiber membrane has a sandwich-like structure in which a dense layer is formed at the center while finger-like structures are formed near the inner and outer walls. The outer diameter and wall thickness of the prepared hollow fiber was 1.38 mm and 0.15 mm, respectively. When the wet 20% H_2 in N_2 and Ar were used as feed gas and sweep gas, respectively, the hydrogen permeation flux of $2.22 \times 10^{-5} \text{ mL cm}^{-2} \text{ min}^{-1}$ was obtained at 900 °C. This value is significantly lower compared to the reported value for $Ni-BaZr_{0.1}Ce_{0.7}Y_{0.2}O_{3-\delta}$ membrane disks [60–63] and asymmetric $Ni-BaZr_{0.1}Ce_{0.7}Y_{0.2}O_{3-\delta}$ membrane disks [86]. It is generally difficult to obtain cermet hollow fiber membranes via phase inversion and sintering route since normal sintering procedure for ceramic hollow fiber may not be applicable to cermet fiber [94].

Membrane surface modification serves as a route to improve the flux performance of hollow fiber when hydrogen transport is limited by the rate of hydrogen exchange on the surface. The increase in surface roughness can provide an increase in the effective membrane surface area. This can be achieved by polishing the membrane surface with different media. A maximum hydrogen flux of $0.53 \text{ mL cm}^{-2} \text{ min}^{-1}$ was reported at 850 °C using a 15 μm -thick $BaCe_{0.95}Tb_{0.05}O_{3-\delta}$ coated $NiO-BaCe_{0.95}Tb_{0.05}O_{3-\delta}$ hollow fiber membrane [96]. This flux was comparable to the hydrogen flux of a 90 μm -thick dual-phase $Ni-BaCe_{0.95}Tb_{0.05}O_{3-\delta}$ disk membrane operated under similar condition [85]. The improved hydrogen flux for $BaCe_{0.95}Tb_{0.05}O_{3-\delta}/NiO-BaCe_{0.95}Tb_{0.05}O_{3-\delta}$ hollow fiber is mainly attributed to the thin transport layer provided by the dense $BaCe_{0.95}Tb_{0.05}O_{3-\delta}$ layer and the large surface area, both of which were featured by the hollow fiber configuration. Ni particles also contributed to the catalyzed hydrogen oxidation into proton and electron on the anode side due to the increase in the amount of three phase boundaries (TPB) [96].

Metal catalysts such as palladium and nickel can be deposited to the membrane surface to improve the surface exchange kinetics and thus the hydrogen fluxes, as in the case of $BaCe_{0.85}Tb_{0.05}Co_{0.1}O_{3-\delta}$ hollow fiber membrane [97]. Palladium is a common catalyst for hydrogen separation membrane while nickel is a typical catalyst for dehydrogenation and hydrogenation reactions. The deposition of palladium catalyst on the surface of $BaCe_{0.85}Tb_{0.05}Co_{0.1}O_{3-\delta}$ hollow fibers was performed by electroless plating. This was followed by a heat treatment at 120 °C in air for 12 h. A 1.88 μm -thick dense palladium layer formed and was well-attached onto the $BaCe_{0.85}Tb_{0.05}Co_{0.1}O_{3-\delta}$ hollow fiber membrane surface. A combined slurry brushing and sintering techniques, on the other hand, was utilized to deposit nickel catalyst, which gave a 99.6 μm -thick porous NiO layer on the hollow fiber membrane surface. A maximum hydrogen permeation flux of $0.269 \text{ mL cm}^{-2} \text{ min}^{-1}$ and $0.42 \text{ mL cm}^{-2} \text{ min}^{-1}$ was obtained at 1000 °C for nickel- and palladium-coated $BaCe_{0.85}Tb_{0.05}Co_{0.1}O_{3-\delta}$ hollow fiber membranes, respectively. For non-modified $BaCe_{0.85}Tb_{0.05}Co_{0.1}O_{3-\delta}$ hollow fiber membrane, a maximum flux of $0.164 \text{ mL cm}^{-2} \text{ min}^{-1}$ was obtained under similar operating conditions. This improvement can be associated to the catalytic effect of both palladium and nickel for hydrogen dissociation. The surface exchange kinetics in the hydrogen permeation can also be enhanced by coating palladium and

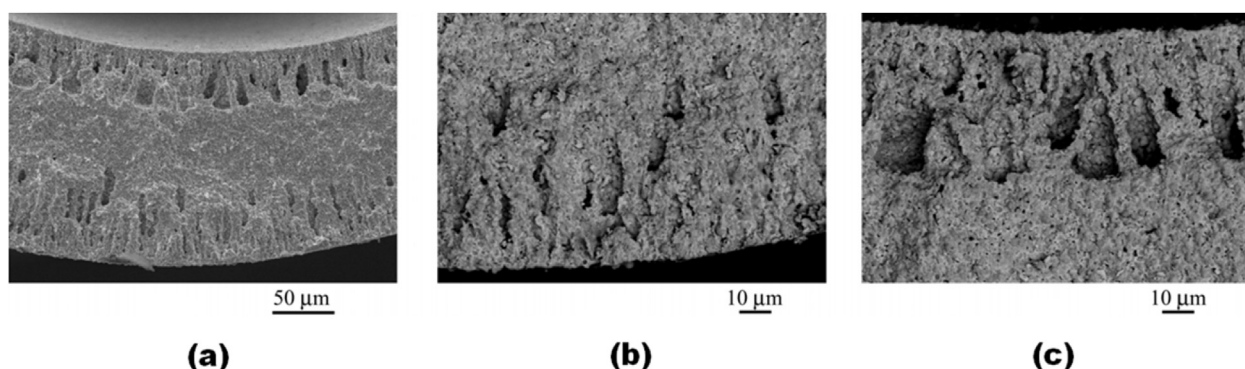


Fig. 12 – Scanning electron microscopy images of $Ni-BaZr_{0.1}Ce_{0.7}Y_{0.2}O_{3-\delta}$ hollow fiber membrane (a) Cross-section; (b) Cross-section near outer surface; and (c) Cross-section near inner surface (Reproduced from [95]).

nickel layers on both sides of the $\text{BaCe}_{0.95}\text{Tb}_{0.05}\text{Co}_{0.1}\text{O}_{3-\delta}$ hollow fiber membrane surfaces.

The effects of surface modification by H_2SO_4 -etching and palladium-coating on the enhancement of hydrogen permeation through the $\text{BaCe}_{0.95}\text{Tb}_{0.05}\text{O}_{3-\delta}$ hollow fiber membranes were reported by Liu and co-workers [98]. The hydrogen permeation flux of the original $\text{BaCe}_{0.95}\text{Tb}_{0.05}\text{O}_{3-\delta}$ hollow fiber membrane at 1000°C was $0.044\text{ mL cm}^{-2}\text{ min}^{-1}$, whereas the palladium-coated membrane showed an improved hydrogen flux by a factor of 4.78, i.e., up to $0.21\text{ mL cm}^{-2}\text{ min}^{-1}$ when operated under similar temperature. A steady increase from

0.021 to $0.158\text{ mL cm}^{-2}\text{ min}^{-1}$ at 1000°C was observed for the H_2SO_4 -etched hollow fiber membrane with palladium-coating on its outer surface. The surface modification by H_2SO_4 -etching however did not lead to the expected enhancement in hydrogen permeation flux but lowered the hydrogen flux instead. The energy dispersive X-ray spectroscopy over the resultant $\text{BaCe}_{0.95}\text{Tb}_{0.05}\text{O}_{3-\delta}$ hollow fiber membrane surface indicated that the sulfur content after 98 wt % H_2SO_4 surface modification reached 5.44 at.% (Fig. 13). This implies that some S-compounds formed and covered the membrane surface; leading to the deterioration of hydrogen permeation

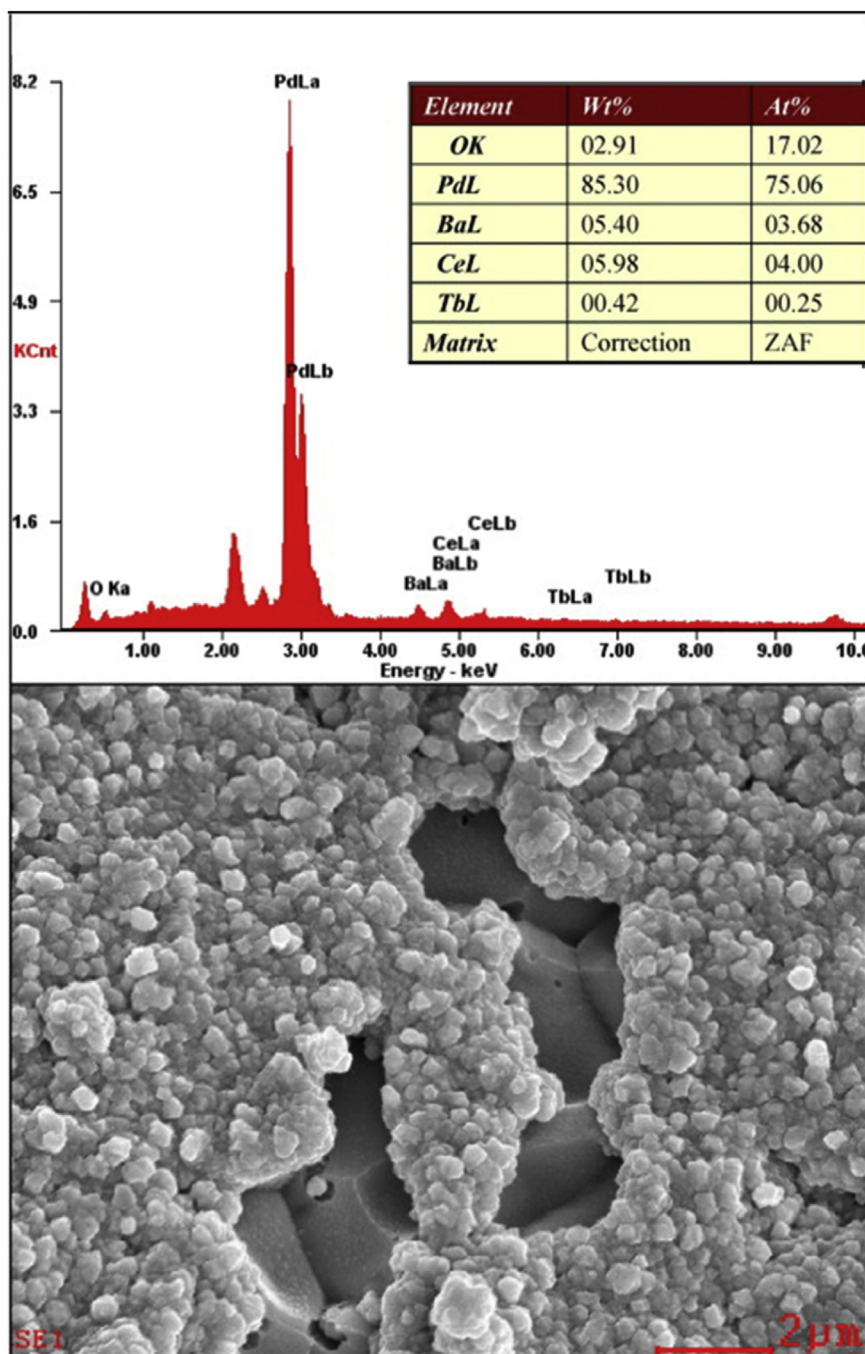


Fig. 13 – Energy dispersive X-ray spectra of the $\text{BaCe}_{0.95}\text{Tb}_{0.05}\text{O}_{3-\delta}$ membrane surface after modification by 98 wt% H_2SO_4 for 10 min, with the whole scanning electron microcopy image as the scanning area (Reproduced from [98]).

performance. The deviation of the metal ratio (Ba:Ce:Tb) from the initial stoichiometric composition of 1:0.95:0.05 to 0.96:1:0.06 suggests that the segregation might occur and some barium content was lost. The newly generated S-compounds are sulfates such as BaSO_4 . These non-ionically conductive sulfates have poisoning effect on the ionic transport and the surface exchange reactions and indicates that H_2SO_4 modification is not suitable for barium-contained perovskite. Moreover, the integrity of the hollow fibers was traded off with the gas-tightness property for hydrogen permeation in the case of HCl use (instead of H_2SO_4).

Surface-modified membranes

As we have discussed in Section [Hollow fiber membranes](#), surface modification can be used to enhance the hydrogen permeation flux of membrane by increasing the surface area through coating a porous layer or by enhancing the surface exchange kinetics (i.e., promote the adsorption and dissociation of hydrogen and/or the association and desorption of proton) through coating a catalyst layer. Hydrogen permeation performances of several surface modified membranes are summarized in [Table 9](#) [74,101–104].

Mather et al. reported that the application of porous platinum catalytic layer on the hydrogen feed-exposed side of a 1.16 mm-thick $\text{Sr}_{0.97}\text{Ce}_{0.9}\text{Yb}_{0.1}\text{O}_{3-\delta}$ membrane improved the hydrogen flux to a maximum $0.04 \text{ mL cm}^{-2} \text{ min}^{-1}$ after 14 h of exposure to 10 vol% H_2 and 90 vol% N_2 at 804°C [104]. The obtained flux was an order of magnitude higher than that of the membrane with similar thickness but without surface modification. The permeation behavior of non-modified membrane was also determined, in which no hydrogen flux was detected after 3 days of operation. The improved performance of the platinum-coated membrane can be ascribed to the catalytic role of platinum on the feed-side surface that promotes the dissociation of hydrogen molecules and the subsequent protonation of the membrane [105]. Similar observation was reported by Li et al. for $\text{BaCe}_{0.9}\text{Mn}_{0.1}\text{O}_{3-\delta}$ membrane coated with a porous platinum black [101]. Likewise, the deposition of a palladium thin film on the surface of $\text{Ni-BaCe}_{0.8}\text{Y}_{0.2}\text{O}_{3-\delta}$ membrane has also resulted in enhanced hydrogen flux performance [102]. Vigen

and Haugsrud investigated the effect of surface kinetics on the hydrogen flux performance of $\text{La}_{0.87}\text{Sr}_{0.13}\text{CrO}_{3-\delta}$ under wet and dry sweep gas conditions by coating a porous platinum catalytic layer on both sides of the membrane [103]. The hydrogen fluxes increased relative to the uncoated $\text{La}_{0.87}\text{Sr}_{0.13}\text{CrO}_{3-\delta}$ membrane; highlighting the major role of surface kinetics. In addition, the effect of platinum-coating became less apparent when 10 vol% CO and 90 vol% CO_2 was used as the feed gas. This suggests that the platinum-coating has small effect on the overall water splitting rate and the resultant oxygen ionic transport from sweep side to feed side.

Challenges and outlook

We have reviewed most of the available laboratory-scale research and development studies on the perovskite-based proton conducting membranes. Despite the apparent progress, the real translation of these works from the bench scale to the pilot production scale would require additional momentum and substantial time and investment for the reasons mentioned below.

Limitations

Most of the reported hydrogen flux performances of perovskite-based proton conducting membranes are still an order of magnitude lower than the required benchmark of $1\text{--}2 \text{ mL cm}^{-2} \text{ min}^{-1}$ at $600\text{--}700^\circ\text{C}$ for commercial applications [106]. Furthermore, the large variation of the reported hydrogen flux performances, even for the same membrane composition. Such variation comes from different synthesis and test conditions such as different membrane thicknesses, different preparation routes and procedures, and different driving forces (i.e., different oxygen partial pressure gradients across the membrane). Different membrane microstructures due to different preparation routes may lead to different protonic and electronic conductivities.

Athayde et al. overviewed various preparation methods for ceramic membrane, i.e., solid-state reaction (SSR) method, the sol-gel method (i.e., EDTA-citric acid (EC) process), the glycine-

Table 9 – Surface modified proton conducting perovskite membranes performance overview for H_2 permeation [74,101–104].

Materials	H_2 flux ($\text{mL cm}^{-2} \text{ min}^{-1}$)	Feed/sweep atmospheres	Temperature ($^\circ\text{C}$)	Thickness (mm)	Note	Ref.
$\text{La}_{0.87}\text{Sr}_{0.13}\text{CrO}_{3-\delta}$	10^{-4}	10% H_2 + 2.5% H_2O + He/Ar	1000	0.55	Disk with Pt layer on both sides Spray pyrolysis provided by Statoil and SINTEF	[103]
$\text{Sr}_{0.97}\text{Ce}_{0.9}\text{Yb}_{0.1}\text{O}_{3-\delta}$	0.044	10% H_2 + 90% N_2 /Ar	804	1.16	Disk with a $\sim 4 \mu\text{m}$ -thick porous Pt catalytic layer on the feed side	[104]
$\text{BaCe}_{0.9}\text{Mn}_{0.1}\text{O}_{3-\delta}$	0.0114	H_2 + N_2 /Ar	800	1.64	Disk with porous thin film of platinum black on feed side	[101]
$\text{Ni-BaCe}_{0.90}\text{Y}_{0.10}\text{O}_{3-\delta}$	0.065	Dry 4% H_2 + 96% He/ H_2 + N_2	900	0.270	Disk with 2 nm-thick Pd layer	[102]
$\text{BaCe}_{0.20}\text{Zr}_{0.70}\text{Y}_{0.10}\text{O}_{3-\delta}$ $\text{Sr}_{0.95}\text{Ti}_{0.90}\text{Nb}_{0.10}\text{O}_{3-\delta}$ (50:50 vol%)	3.49×10^{-2}	Dry 4% H_2 + 96% He/Dry Ar	800	1	Disk with 100 nm Pd layer as catalyst	[74]

nitrate combustion process, and the chemical co-precipitation method [42]. Powders synthesized via different processes have different particle sizes, sintering behavior, and chemical compositions. All these factors could lead to different microstructures following the sintering of “green” membranes at elevated temperatures. Thirdly, the high cost and complex membrane preparation procedure. Solid state reaction (SSR) route is generally considered as high cost route due to the high cost metal oxide raw materials and the involvement of multi-step processes. Likewise, for sol-gel route, pH-controlling step is required for complete complexation. Advanced synthesis processes are therefore more attractive in the perspective of lowering the sintering temperature, which is energy intensive. The use of rare and expensive metals such as palladium and platinum as catalysts to overcome the surface exchange limitation of the membrane is not practical. This can be addressed by replacing these metals with cheaper more abundant transition metals such as iron and nickel.

Another challenge lies in the highly complex and expensive characterization procedure for perovskite powders and membranes. Different complementary techniques such as scanning electron microscopy (SEM), energy dispersive X-ray (EDX) analysis, powder X-ray diffraction (XRD), four-probe DC technique, electrical conductivity relaxation (ECR), and hydrogen permeation test are required, which involve significant upfront investment, extensive training, and high operation and maintenance cost. There certainly is a need for low-cost analytical methods that allows faster and simple “screening” analysis of perovskite powders and membranes.

In severe operating conditions (e.g., elevated temperatures), the chemical reactivity towards the existing gas species (i.e., water vapor, CO₂, etc.) increases. This may lead to mechanical, chemical, and structural instability of the membranes and premature performance loss. While considerable progress has been made to advance the membrane materials and performances, it remains difficult to obtain an ideal membrane that features simultaneously high hydrogen permeation flux and high chemical, mechanical, and structural stability.

Future insights

Among various perovskite membranes summarized in this review, BaCeO₃-based materials are regarded as benchmark materials for their high and nearly pure proton conductivity [107]. Nonetheless, doped BaCeO₃ materials are chemically unstable in acidic and amphoteric gases, i.e., CO₂, SO₂, and H₂O [108]. Reaction with these gases leads to the formation of carbonates, sulfates, and hydroxides. The poor chemical stability of BaCeO₃ is not surprising given its perovskite structure instability below 631 °C [109]. BaCeO₃ stability is lower than those of its constituent oxides. Partial replacement of Ce⁴⁺ by Zr⁴⁺, which leads to perovskite composition of BaCe_{1-x-y}Zr_xY_yO_{3-δ}, has been considered as an effective method to improve its chemical stability. This stability enhancement is however obtained at the cost of the proton conductivity and sinterability degradation [110].

Matsumoto et al. discussed the correlation between the electrical conductivity and the chemical stability of BaCeO₃-based proton conductors with different trivalent dopants

[111]. They underscore the importance of stability or aging tests since the lifetime duration of the membrane is one of its practical economic indicator. Slodczyk et al. tested the chemical and structural stability of four proton conducting perovskite membranes (i.e., BaZr_{0.9}Yb_{0.1}O_{3-δ}, SrZr_{0.9}Yb_{0.1}O_{3-δ}, BaZr_{0.25}In_{0.75}O_{3-δ}, and BaCe_{0.5}Zr_{0.3}Y_{0.16}Zn_{0.04}O_{3-δ}) by *in situ* and *ex situ* autoclave Raman microscopy [112]. They reported that the operating conditions (i.e., temperature, pressure, and permeation duration) affect the membrane stability. Sr-based membrane was found to be more structurally, mechanically, and chemically stable than the Ba-based membrane. Despite the higher hydrogen permeation flux for hollow fiber relative to the other membrane configuration, the practicality of a hollow fiber membrane relies upon its mechanical strength. Within this context, the sintering conditions such as temperature and membrane materials generally determine the mechanical properties of the hollow fiber membranes [92]. In the near future, three-dimensional (3D) printing techniques, also known as additive manufacturing or rapid prototyping can open the door to the advancement of membrane capabilities [113,114]. Since 3D printing of membranes is currently still in its infancy, there is much more work to be performed to make the technology cost competitive and comparable to typical perovskite membrane fabrication methods. At present, the work on 3D printing for gas separation membranes has not been reported.

The majority of research attempts in the perovskite-based proton conducting membranes have been directed towards developing new compositions with enhanced permeation and chemical stability. Little emphasis has been paid to the materials and system cost. Since current ceramic processing technology exhibits limitations in terms of complex powder synthesis and low to medium reproducibility. Further cost and environmental impact assessments should be made into the existing perovskite membrane materials and processes to identify the main cost drivers. Such assessments can provide insights for the following process optimization. In this light, DeSantis et al. performed a techno-economic analysis for metal-organic framework (MOF) adsorbents for hydrogen and natural gas storage to understand the cost drivers for large-scale MOF synthesis and highlight potential pathways to reduce MOF production cost at an industrially relevant scale [115].

Since hydrogen permeation performances are influenced by the membrane material, the membrane geometry, and the operating conditions, i.e., temperature and upstream and downstream hydrogen partial pressures, determining the optimum membrane operation conditions and design may involve time consuming experiments. Modeling and simulation studies can assist to reduce the experimental costs in evaluating the dominant operation and design variables. Such works on various perovskite-based proton conducting membranes have been performed [22,45,116–121]. Guan et al. used a simplified equation to calculate the hydrogen flux of SrCe_{0.95}Y_{0.05}O_{3-δ} in a short-circuited configuration, in which the proton conductivity is assumed to be constant [116]. This assumption however contradicts the fact that there is a proton concentration gradient in the hydrogen permeation across the membrane. As a result, the hydrogen flux predicted by their simplified equation did not agree with the experimental results.

Song et al. utilized a point defect model to describe the functional dependence of defect species in $\text{SrCe}_{0.95}\text{Y}_{0.05}\text{O}_{3-\delta}$ on hydrogen, water vapor, and oxygen partial pressure [22]. The hydrogen permeation equations derived from the chemical diffusion theory were solved using a numerical modeling method. Matsuka et al. simulated the hydrogen permeation flux performance of $\text{SrCe}_{0.95}\text{Yb}_{0.05}\text{O}_{3-\delta}$ and $\text{SrCe}_{0.95}\text{Tm}_{0.05}\text{O}_{3-\delta}$ membranes and compared them with the experimental values [45]. Comparison between simulated and experimental data (i.e., in wet hydrogen atmosphere with known vapor pressures) were in good agreement. In their earlier works, Matsuka et al. [117,120] adopted the method described by Poulsen [122] and Song et al. [22] to predict the hydrogen permeation flux of $\text{SrCe}_{0.95}\text{Yb}_{0.05}\text{O}_{3-\delta}$ and $\text{SrCe}_{0.95}\text{Tm}_{0.05}\text{O}_{3-\delta}$ membranes and compared the simulated data to the experimental values (i.e., in dry hydrogen atmosphere with unknown vapor pressures) from Hamakawa et al. [82] and Cheng et al. [38]. The disagreement between the predicted and experimental values was attributed to the undefined water vapor partial pressures utilized in the experiments. Norby and Haugsrud claimed that the hydrogen permeation measurements in a dry, reducing hydrogen atmosphere may not be achievable and that the membrane is unstable in dry hydrogen [123].

Zhang et al. developed a mathematical model for $\text{Ni-BaCe}_{1-x}\text{Y}_x\text{O}_{3-\delta}/\text{BaCe}_{1-x}\text{Zr}_y\text{Y}_x\text{O}_{3-\delta}$ dual-phase membrane to correlate the hydrogen permeation flux performance to the geometric parameters of membranes and the experimental conditions [119]. Their model utilized the percolation theory to describe the membrane microstructure in the dual-phase membrane. The simulated hydrogen flux performance of an asymmetric dual-phase membrane with a composition of $\text{Ni-BaCe}_{1-x}\text{Zr}_y\text{Y}_x\text{O}_{3-\delta}$ was in good agreement with the experimental values [124]. Gas transport in porous support, bulk diffusion in dense layer, surface exchange at both membrane surfaces, and hydrogen permeation from Ni phase were considered in the developed model. While the research on modeling and simulation has progressed, further work should be directed to the application of more advanced two- and three-dimensional models.

Conclusions

Numerous research works have been performed on the perovskite-based oxides as hydrogen separation membrane materials. For perovskite-based membranes to become feasible and economically practical, numerous challenges must be solved. The most important are the development of membrane material with high permeability, high electrical conductivity, and high chemical, mechanical, and structural stability using low-cost raw materials, reproducible preparation, and characterization methods. To date, however, no single material has met all these requirements for application as a practical hydrogen separation membrane despite BaCeO_3 -based materials being regarded as benchmark materials for their high and nearly pure proton conductivity. Membranes with high chemical and structural stability generally deliver lower hydrogen permeation fluxes compared to the membranes with low chemical and structural stability. Future advancement on perovskite-based hydrogen

separation membranes can also be made by exploring technological possibilities that have not yet been applied such as 3D-printing. Moreover, the flexibility of the perovskite structure with respect to doping and partial substitution of A- or B-site cations warrant their potential for further study.

Acknowledgment

Siti Salwa Hashim and Jaka Sunarso would like to acknowledge the funding provided by Swinburne University of Technology Sarawak Campus (SUTS) through Swinburne Sarawak Research Grant (SSRG) (Account number: 2–5534).

REFERENCES

- [1] Winter C-J. Hydrogen energy — abundant, efficient, clean: a debate over the energy-system-of-change. *Int J Hydrogen Energy* 2009;34:S1–52.
- [2] Grey E. German state thrusts hydrogen-powered hyrail into the spotlight. *Railw Technol* June 2016;21.
- [3] Gosden E. UK homes could be heated by hydrogen under plan to tackle global warming. *Telegraph* April 2016;9.
- [4] Obe M. Tokyo hopes to make hydrogen power the star of the 2020 Olympics. *Wall St J* September 2015;11.
- [5] Hydrogen on the rise. *Nat Energy* August 2016;4.
- [6] Ogden JM. Review of small stationary reformers for hydrogen production. 2001.
- [7] Adhikari S, Fernando S. Hydrogen membrane separation techniques. *Ind Eng Chem Res* 2006;45:875–81.
- [8] Al-Mufachi NA, Rees NV, Steinberger-Wilkens R. Hydrogen selective membranes: a review of palladium-based dense metal membranes. *Renew Sustain Energy Rev* 2015;47:540–51.
- [9] Bredesen R, Jordal K, Bolland O. High-temperature membranes in power generation with CO_2 capture. *Chem Eng Process* 2004;43:1129–58.
- [10] Caro J, Noack M, Kölsch P, Schäfer R. Zeolite membranes — state of their development and perspective. *Micropor Mesopor Mater* 2000;38:3–24.
- [11] Ismail AF, David LIB. A review on the latest development of carbon membranes for gas separation. *J Membr Sci* 2001;193:1–18.
- [12] Yun S, Ted Oyama S. Correlations in palladium membranes for hydrogen separation: a review. *J Membr Sci* 2011;375:28–45.
- [13] Gallucci F, Fernandez E, Corengia P, van Sint Annaland M. Recent advances on membranes and membrane reactors for hydrogen production. *Chem Eng Sci* 2013;92:40–66.
- [14] Iwahara H, Esaka T, Uchida H, Maeda N. Proton conduction in sintered oxides and its application to steam electrolysis for hydrogen production. *Solid State Ionics* 1981;3:359–63.
- [15] Megaw HD. Structures of oxides. *Crystal structures: a working approach*. Philadelphia: Saunders; 1973. p. 217–9.
- [16] Vendrell X. Perovskite structure. In: *Explorer Materials*; 2014. <https://explorermaterials.wordpress.com/basic-concepts/perovskite-structure/> [Accessed 28 June 2018].
- [17] Bhalla SA, Guo R, Roy R. The perovskite structure — a review of its role in ceramic science and technology. *Mater Res Innov* 2000;4:3–26.
- [18] Sunarso J, Baumann S, Serra JM, Meulenberg WA, Liu S, Lin YS, et al. Mixed ionic–electronic conducting (MIEC) ceramic-based membranes for oxygen separation. *J Membr Sci* 2008;320:13–41.

- [19] Shannon R. Revised effective ionic radii and systematic studies of interatomic distances in halides and chalcogenides. *Acta Crystallogr A* 1976;32:751–67.
- [20] Bhalla A, Guo R, Roy R. The perovskite structure—a review of its role in ceramic science and technology. *Mater Res Innovat* 2000;4:3–26.
- [21] Qi X, Lin YS. Electrical conduction and hydrogen permeation through mixed proton–electron conducting strontium cerate membranes. *Solid State Ionics* 2000;130:149–56.
- [22] Song SJ, Wachsman ED, Rhodes J, Dorris SE, Balachandran U. Numerical modeling of hydrogen permeation in chemical potential gradients. *Solid State Ionics* 2003;164:107–16.
- [23] Kreuer KD. Proton-conducting oxides. *Annu Rev Mater Res* 2003;33:333–59.
- [24] Stotz VS, Wagner C. *Ber Bunsenges Phys Chem* 1967;70:781.
- [25] Proton Conducting Ceramics. Inside Mines; 2017. <http://inside.mines.edu/PROTON-CONDUCTING-CERAMICS> [Accessed 28 June 2018].
- [26] Iwahara H. High temperature proton conductors based on perovskite-type oxides. In: Philippe C, editor. *Proton conductors: solids, membranes and gels - materials and devices*. Cambridge: Cambridge University Press; 1992. p. 122–37.
- [27] Norby T, Larring Y. Concentration and transport of protons in oxides. *Curr Opin Solid State Mater Sci* 1997;2:593–9.
- [28] Wen X. Mixed proton-electron conducting oxides for high temperature hydrogen separation membrane. University of Iso; 2013.
- [29] Ryu KH, Haile SM. Chemical stability and proton conductivity of doped BaCeO₃–BaZrO₃ solid solutions. *Solid State Ionics* 1999;125:355–67.
- [30] Kannan R, Singh K, Gill S, Fürstenhaupt T, Thangadurai V. Chemically stable proton conducting doped BaCeO₃ -No more fear to SOFC wastes. *Sci Rep* 2013;3:2138.
- [31] Wu J, Davies RA, Islam MS, Haile SM. Atomistic study of doped BaCeO₃: Dopant site-selectivity and cation nonstoichiometry. *Chem Mater* 2005;17:846–51.
- [32] Zhao F, Liu Q, Wang S, Brinkman K, Chen F. Synthesis and characterization of BaIn_{0.3–x}Y_xCe_{0.7}O_{3–δ} (x = 0, 0.1, 0.2, 0.3) proton conductors. *Int J Hydrogen Energy* 2010;35:4258–63.
- [33] Qi X, Lin YS. Electrical conducting properties of proton-conducting terbium-doped strontium cerate membrane. *Solid State Ionics* 1999;120:85–93.
- [34] Hamakawa S, Hibino T, Iwahara H. Electrochemical hydrogen permeation in a proton-hole mixed conductor and its application to a membrane reactor. *J Electrochem Soc* 1994;141:1720–5.
- [35] Liu Y, Tan X, Li K. Mixed conducting ceramics for catalytic membrane processing. *Catal Rev* 2006;48:145–98.
- [36] Norby T. Solid-state protonic conductors: principles, properties, progress and prospects. *Solid State Ionics* 1999;125:1–11.
- [37] Wei X, Knip J, Lin YS. Hydrogen permeation through terbium doped strontium cerate membranes enabled by presence of reducing gas in the downstream. *J Membr Sci* 2009;345:201–6.
- [38] Cheng S, Gupta VK, Lin JYS. Synthesis and hydrogen permeation properties of asymmetric proton-conducting ceramic membranes. *Solid State Ionics* 2005;176:2653–62.
- [39] Knight KS, Bonanos N. The crystal structures of some doped and undoped alkaline earth cerate perovskites. *Mater Res Bull* 1995;30:347–56.
- [40] Arima M, Kakihana M, Nakamura Y, Yashima M, Yoshimura M. Polymerized complex route to barium titanate powders using barium-titanium mixed-metal citric acid complex. *J Am Ceram Soc* 1996;79:2847–56.
- [41] Cousin P, Ross RA. Preparation of mixed oxides: a review. *Mater Sci Eng A* 1990;130:119–25.
- [42] Athayde DD, Souza DF, Silva AMA, Vasconcelos D, Nunes EHM, Diniz da Costa JC, et al. Review of perovskite ceramic synthesis and membrane preparation methods. *Ceram Int* 2016;42:6555–71.
- [43] Song SJ, Wachsman ED, Rhodes J, Dorris SE, Balachandran U. Hydrogen permeability of SrCe_{1–x}M_xO_{3–δ} (x = 0.05, M = Eu, Sm). *Solid State Ionics* 2004;167:99–105.
- [44] Knip J, Lin YS. Effect of zirconium doping on hydrogen permeation through strontium cerate membranes. *Ind Eng Chem Res* 2010;49:2768–74.
- [45] Matsuka M, Braddock RD, Matsumoto H, Sakai T, Agranovski IE, Ishihara T. Experimental and theoretical studies of hydrogen permeation for doped strontium cerates. *Solid State Ionics* 2010;181:1328–35.
- [46] Yuan WH, Mao LL, Li L. Novel SrCe_{0.75}Zr_{0.20}Tm_{0.05}O_{3–δ} membrane for hydrogen separation. *Chin Chem Lett* 2010;21:369–72.
- [47] Yuan W, Xiao C, Li L. Hydrogen permeation and chemical stability of In-doped SrCe_{0.95}Tm_{0.05}O_{3–δ} membranes. *J Alloy Comp* 2014;616:142–7.
- [48] Tan X, Tan X, Yang N, Meng B, Zhang K, Liu S. High performance BaCe_{0.8}Y_{0.2}O_{3–δ} (BCY) hollow fibre membranes for hydrogen permeation. *Ceram Int* 2014;40:3131–8.
- [49] Cai M, Liu S, Efimov K, Caro J, Feldhoff A, Wang H. Preparation and hydrogen permeation of BaCe_{0.95}Nd_{0.05}O_{3–δ} membranes. *J Membr Sci* 2009;343:90–6.
- [50] Zhang H, Wilhite BA. Electrical conduction and hydrogen permeation investigation on iron-doped barium zirconate membrane. *J Membr Sci* 2016;512:104–10.
- [51] Escolástico S, Ivanova M, Solis C, Roitsch S, Meulenberg WA, Serra JM. Improvement of transport properties and hydrogen permeation of chemically-stable proton-conducting oxides based on the system BaZr_{1–x-y}Y_xMyO_{3–δ}. *RSC Adv* 2012;2:4932–43.
- [52] Bonanos N. Transport properties and conduction mechanism in high-temperature protonic conductors. *Solid State Ionics* 1992;53:967–74.
- [53] Wei X, Lin YS. Protonic and electronic conductivities of terbium doped strontium cerates. *Solid State Ionics* 2008;178:1804–10.
- [54] Bi L, Zhang S, Zhang L, Tao Z, Wang H, Liu W. Indium as an ideal functional dopant for a proton-conducting solid oxide fuel cell. *Int J Hydrogen Energy* 2009;34:2421–5.
- [55] Dang J, Zhu Z, Qian J, Liu W. A stable BaCe_{0.7}Ta_{0.1}In_{0.2}O_{3–δ} electrolyte membrane for proton-conducting solid oxide fuel cells. *Ceram Int* 2013;39:4287–92.
- [56] Chen FL, Sørensen OT, Meng GY, Peng DK. Preparation of Nd-doped BaCeO₃ proton-conducting ceramic and its electrical properties in different atmospheres. *J Eur Ceram Soc* 1998;18:1389–95.
- [57] Balachandran U, Lee TH, Chen L, Song SJ, Picciolo JJ, Dorris SE. Hydrogen separation by dense cermet membranes. *Fuel* 2006;85:150–5.
- [58] Fang S, Brinkman KS, Chen F. Hydrogen permeability and chemical stability of Ni–BaZr_{0.1}Ce_{0.7}Y_{0.1}Yb_{0.1}O_{3–δ} membrane in concentrated H₂O and CO₂. *J Membr Sci* 2014;467:85–92.
- [59] Wei Y, Xue J, Fang W, Chen Y, Wang H, Caro J. Enhanced stability of Zr-doped Ba(CeTb)O_{3–δ}-Ni cermet membrane for hydrogen separation. *Chem Commun* 2015;51:11619–21.
- [60] Kim H, Kim B, Lee J, Ahn K, Kim H-R, Yoon KJ, et al. Microstructural adjustment of Ni–BaCe_{0.9}Y_{0.1}O_{3–δ} cermet membrane for improved hydrogen permeation. *Ceram Int* 2014;40:4117–26.
- [61] Zuo C, Dorris SE, Balachandran U, Liu M. Effect of Zr-doping on the chemical stability and hydrogen permeation of the

- Ni-BaCe_{0.8}Y_{0.2}O_{3- α} mixed protonic-electronic conductor. *Chem Mater* 2006;18:4647–50.
- [62] Zuo C, Lee TH, Dorris SE, Balachandran U, Liu M. Composite Ni-Ba(Zr_{0.1}Ce_{0.7}Y_{0.2})O₃ membrane for hydrogen separation. *J Power Sources* 2006;159:1291–5.
- [63] Fang S, Bi L, Yang C, Yan L, Chen C, Liu W. H₂S poisoning and regeneration of Ni–BaZr_{0.1}Ce_{0.7}Y_{0.2}O_{3- δ} at intermediate temperature. *J Alloy Comp* 2009;475:935–9.
- [64] Fang S, Brinkman K, Chen F. Unprecedented CO₂-promoted hydrogen permeation in Ni-BaZr_{0.1}Ce_{0.7}Y_{0.1}Yb_{0.1}O_{3- δ} membrane. *ACS Appl Mater Interfaces* 2014;6:725–30.
- [65] Zhu Z, Sun W, Dong Y, Wang Z, Shi Z, Zhang Q, et al. Evaluation of hydrogen permeation properties of Ni–Ba(Zr_{0.7}Pr_{0.1}Y_{0.2})O_{3- δ} cermet membranes. *Int J Hydrogen Energy* 2014;39:11683–9.
- [66] Jeon SY, Lim DK, Choi MB, Wachsman ED, Song SJ. Hydrogen separation by Pd–CaZr_{0.9}Y_{0.1}O_{3- δ} cermet composite membranes. *Sep Purif Technol* 2011;79:337–41.
- [67] Tsai Y-C, Lin C-C, Lin W-L, Wang J-H, Chen S-Y, Lin P, et al. Palladium based cermet composite for hydrogen separation at elevated temperature. *J Power Sources* 2015;274:965–70.
- [68] Rosensteel WA, Sullivan NP. Fabrication and hydrogen permeation through novel BaZr_{0.9}Y_{0.1}O_{3- δ} –Cu composite ceramic-metallic membranes. *Int J Hydrogen Energy* 2017;42:4216–23.
- [69] Islam QA, Raja MW, Basu RN. Zr- and Tb-doped barium cerate-based cermet membrane for hydrogen separation application. *J Am Ceram Soc* 2017;1–8.
- [70] Ruiz-Trejo E, Zhou Y, Brandon NP. On the manufacture of silver–BaCe_{0.5}Zr_{0.3}Y_{0.16}Zn_{0.04}O_{3- δ} composites for hydrogen separation membranes. *Int J Hydrogen Energy* 2015;40:4146–53.
- [71] German RM, Suri P, Park SJ. Review: liquid phase sintering. *J Mater Sci* 2009;44:1–39.
- [72] Wang T, Zhang H, Meng B, Wang X, Sunarso J, Tan X, et al. SrCe_{0.95}Y_{0.05}O_{3- δ} –ZnO dual-phase membranes for hydrogen permeation. *RSC Adv* 2016;6:36786–93.
- [73] Sekino T, Nakajima T, Ueda S, Niihara K. Reduction and sintering of a nickel–dispersed-alumina composite and its properties. *J Am Ceram Soc* 1997;80:1139–48.
- [74] Fish JS, Ricote S, O'Hayre R, Bonanos N. Electrical properties and flux performance of composite ceramic hydrogen separation membranes. *J Mater Chem A* 2015;3:5392–401.
- [75] Rosensteel WA, Ricote S, Sullivan NP. Hydrogen permeation through dense BaCe_{0.8}Y_{0.2}O_{3- δ} –Ce_{0.8}Y_{0.2}O_{2- δ} composite-ceramic hydrogen separation membranes. *Int J Hydrogen Energy* 2016;41:2598–606.
- [76] Rebollo E, Mortalo C, Escolastico S, Boldrini S, Barison S, Serra JM, et al. Exceptional hydrogen permeation of all-ceramic composite robust membranes based on BaCe_{0.65}Zr_{0.26}Y_{0.15}O_{3- δ} and Y- or Gd-doped ceria. *Energy Environ Sci* 2015;8:3675–86.
- [77] Escolastico S, Solis C, Kjolseth C, Serra JM. Outstanding hydrogen permeation through CO₂-stable dual-phase ceramic membranes. *Energy Environ Sci* 2014;7:3736–46.
- [78] Wang H, Peng R, Wu X, Hu J, Xia C. Sintering behavior and conductivity study of yttrium-doped BaCeO₃–BaZrO₃ solid solutions using ZnO additives. *J Am Ceram Soc* 2009;92:2623–9.
- [79] Schmale K, Daniels M, Buchheit A, Grünebaum M, Haase L, Kooops S, et al. Influence of zinc oxide on the conductivity of ceria. *J Electrochem Soc* 2013;160:F1081–7.
- [80] Kim J-H, Kang Y-M, Kim B-G, Lee S-H, Hwang K-T. Preparation of dense composite membrane with Ba-cerate conducting oxide and rapidly solidified Zr-based alloy. *Int J Hydrogen Energy* 2011;36:10129–35.
- [81] Wei Y, Xue J, Wang H, Caro J. Hydrogen permeability and stability of BaCe_{0.85}Tb_{0.05}Zr_{0.1}O_{3- δ} asymmetric membranes. *J Membr Sci* 2015;488:173–81.
- [82] Hamakawa S, Li L, Li A, Iglesia E. Synthesis and hydrogen permeation properties of membranes based on dense SrCe_{0.95}Yb_{0.05}O_{3- α} thin films. *Solid State Ionics* 2002;148:71–81.
- [83] Li J, Yoon H, Wachsman ED. Hydrogen permeation through thin supported SrCe_{0.7}Zr_{0.2}Eu_{0.1}O_{3- δ} membranes; dependence of flux on defect equilibria and operating conditions. *J Membr Sci* 2011;381:126–31.
- [84] Hung IM, Chiang Y-J, Jang JS-C, Lin J-C, Lee S-W, Chang J-K, et al. The proton conduction and hydrogen permeation characteristic of Sr(Ce_{0.6}Zr_{0.4})_{0.85}Y_{0.15}O_{3- δ} ceramic separation membrane. *J Eur Ceram Soc* 2015;35:163–70.
- [85] Meng X, Song J, Yang N, Meng B, Tan X, Ma Z-F, et al. Ni–BaCe_{0.95}Tb_{0.05}O_{3- δ} cermet membranes for hydrogen permeation. *J Membr Sci* 2012;401–402:300–5.
- [86] Zhu Z, Sun W, Yan L, Liu W, Liu W. Synthesis and hydrogen permeation of Ni-Ba(Zr_{0.1}Ce_{0.7}Y_{0.2})O_{3- δ} metal-ceramic asymmetric membranes. *Int J Hydrogen Energy* 2011;36:6337–42.
- [87] Liu M, Sun W, Li X, Feng S, Ding D, Chen D, et al. High-performance Ni–BaZr_{0.1}Ce_{0.7}Y_{0.1}Yb_{0.1}O_{3- δ} (BZCYYb) membranes for hydrogen separation. *Int J Hydrogen Energy* 2013;38:14743–9.
- [88] Yoon H, Song S-J, Oh T, Li J, Duncan KL, Wachsman ED. Fabrication of thin-film SrCe_{0.9}Eu_{0.1}O_{3- δ} hydrogen separation membranes on Ni–SrCeO₃ porous tubular supports. *J Am Ceram Soc* 2009;92:1849–52.
- [89] An R, Song J, Li Y, Tan X, Sunarso J, Zhang C, et al. Bundling strategy to simultaneously improve the mechanical strength and oxygen permeation flux of the individual perovskite hollow fiber membranes. *J Membr Sci* 2017;527:137–42.
- [90] Chi Y, Li T, Wang B, Wu Z, Li K. Morphology, performance and stability of multi-bore capillary La_{0.6}Sr_{0.4}Co_{0.2}Fe_{0.8}O_{3- δ} oxygen transport membranes. *J Membr Sci* 2017;529:224–33.
- [91] Zhu J, Wang T, Song Z, Liu Z, Zhang G, Jin W. Enhancing oxygen permeation via multiple types of oxygen transport paths in hepta-bore perovskite hollow fibers. *AIChE J* 2017;63:4273–7.
- [92] Liu Y, Tan X, Li K. SrCe_{0.95}Yb_{0.05}O_{3- α} (SCYb) hollow fibre membrane: preparation, characterization and performance. *J Membr Sci* 2006;283:380–5.
- [93] Tan X, Song J, Meng X, Meng B. Preparation and characterization of BaCe_{0.95}Tb_{0.05}O_{3- α} hollow fibre membranes for hydrogen permeation. *J Eur Ceram Soc* 2012;32:2351–7.
- [94] Song J, Li L, Tan X, Li K. BaCe_{0.85}Tb_{0.05}Co_{0.1}O_{3- δ} perovskite hollow fibre membranes for hydrogen/oxygen permeation. *Int J Hydrogen Energy* 2013;38:7904–12.
- [95] Yang C-l, Xu Q-m, Zhu Z-w, Liu W. Hydrogen permeation performance of Ni-BaZr_{0.1}Ce_{0.7}Y_{0.2}O_{3- δ} metal-ceramic hollow fiber membrane. *Chin J Chem Phys* 2012;25:125–8.
- [96] Meng X, Shang Y, Meng B, Yang N, Tan X, Sunarso J, et al. Bi-functional performances of BaCe_{0.95}Tb_{0.05}O_{3- δ} -based hollow fiber membranes for power generation and hydrogen permeation. *J Eur Ceram Soc* 2016;36:4123–9.
- [97] Song J, Kang J, Tan X, Meng B, Liu S. Proton conducting perovskite hollow fibre membranes with surface catalytic modification for enhanced hydrogen separation. *J Eur Ceram Soc* 2016;36:1669–77.
- [98] Song J, Meng B, Tan X, Liu S. Surface-modified proton conducting perovskite hollow fibre membranes by Pd-coating for enhanced hydrogen permeation. *Int J Hydrogen Energy* 2015;40:6118–27.
- [99] Liu S, Tan X, Li K, Hughes R. Preparation and characterisation of SrCe_{0.95}Yb_{0.05}O_{2.975} hollow fibre membranes. *J Membr Sci* 2001;193:249–60.

- [100] Liu Y, Li K. Preparation of $\text{SrCe}_{0.95}\text{Yb}_{0.05}\text{O}_{3-\alpha}$ hollow fibre membranes: study on sintering processes. *J Membr Sci* 2005;259:47–54.
- [101] Li GT, Xiong GX, Sheng SS, Yang WS. Hydrogen permeation properties of perovskite-type $\text{BaCe}_{0.9}\text{Mn}_{0.1}\text{O}_{3-\delta}$ dense ceramic membrane. *Chin Chem Lett* 2001;12:937–40.
- [102] Zhang G, Dorris S, Balachandran U, Liu M. Effect of Pd coating on hydrogen permeation of Ni-barium cerate mixed conductor. *Electrochem Solid State Lett* 2002;5:J5–7.
- [103] Vigen CK, Haugsrud R. Hydrogen flux in $\text{La}_{0.87}\text{Sr}_{0.13}\text{CrO}_{3-\delta}$. *J Membr Sci* 2014;468:317–23.
- [104] Mather GC, Poulidi D, Thursfield A, Pascual MJ, Jurado JR, Metcalfe IS. Hydrogen-permeation characteristics of a SrCeO_3 -based ceramic separation membrane: thermal, ageing and surface-modification effects. *Solid State Ionics* 2010;181:230–5.
- [105] Potter AR, Baker RT. Impedance studies on $\text{Pt}|\text{SrCe}_{0.95}\text{Yb}_{0.05}\text{O}_3|\text{Pt}$ under dried and humidified air, argon and hydrogen. *Solid State Ionics* 2006;177:1917–24.
- [106] Ivanova ME, Escolástico S, Balaguer M, Palisaitis J, Sohn YJ, Meulenber WA, et al. Hydrogen separation through tailored dual phase membranes with nominal composition $\text{BaCe}_{0.8}\text{Eu}_{0.2}\text{O}_{3-\delta}$ - $\text{Ce}_{0.8}\text{Y}_{0.2}\text{O}_{2-\delta}$ at intermediate temperatures. *Sci Rep* 2016;6:34773.
- [107] Iwahara H, Uchida H, Ono K, Ogaki K. Proton conduction in sintered oxides based on BaCeO_3 . *J Electrochem Soc* 1988;135:529–33.
- [108] Kreuer KD. On the development of proton conducting materials for technological applications. *Solid State Ionics* 1997;97:1–15.
- [109] Gopalan S, Virkar AV. Thermodynamic stabilities of SrCeO_3 and BaCeO_3 using a molten salt method and galvanic cells. *J Electrochem Soc* 1993;140:1060–5.
- [110] Zuo C, Zha S, Liu M, Hatano M, Uchiyama M. $\text{Ba}(\text{Zr}_{0.1}\text{Ce}_{0.7}\text{Y}_{0.2})\text{O}_{3-\delta}$ as an electrolyte for low-temperature solid-oxide fuel cells. *Adv Mater* 2006;18:3318–20.
- [111] Matsumoto H, Kawasaki Y, Ito N, Enoki M, Ishihara T. Relation between electrical conductivity and chemical stability of BaCeO_3 -based proton conductors with different trivalent dopants. *Electrochem Solid State Lett* 2007;10:B77–80.
- [112] Slodczyk A, Zaafrani O, Sharp MD, Kilner JA, Dabrowski B, Lacroix O, et al. Testing the chemical/structural stability of proton conducting perovskite ceramic membranes by in situ/ex situ autoclave Raman microscopy. *Membranes* 2013;3:311–30.
- [113] Lee J-Y, Tan WS, An J, Chua CK, Tang CY, Fane AG, et al. The potential to enhance membrane module design with 3D printing technology. *J Membr Sci* 2016;499:480–90.
- [114] Low Z-X, Chua YT, Ray BM, Mattia D, Metcalfe IS, Patterson DA. Perspective on 3D printing of separation membranes and comparison to related unconventional fabrication techniques. *J Membr Sci* 2017;523:596–613.
- [115] DeSantis D, Mason JA, James BD, Houchins C, Long JR, Veenstra M. Techno-economic analysis of metal–organic frameworks for hydrogen and natural gas storage. *Energy Fuels* 2017;31:2024–32.
- [116] Guan J, Dorris SE, Balachandran U, Meilin L. Transport properties of $\text{SrCe}_{0.95}\text{Y}_{0.05}\text{O}_{3-\delta}$ and its application for hydrogen separation. *Solid State Ionics* 1998;110:303–10.
- [117] Matsuka M, Braddock R, Agranovski I. Numerical study of hydrogen permeation flux in $\text{SrCe}_{0.95}\text{Yb}_{0.05}\text{O}_{3-\alpha}$ and $\text{SrCe}_{0.95}\text{Tm}_{0.05}\text{O}_{3-\alpha}$. *Solid State Ionics* 2007;178:1011–9.
- [118] Li L, Iglesia E. Modeling and analysis of hydrogen permeation in mixed proton–electronic conductors. *Chem Eng Sci* 2003;58:1977–88.
- [119] Zhang Q, Liu T, Zhu Z, Hao L, Liu W. Modeling of hydrogen permeation for Ni-ceramic proton conductor composite membrane with symmetric structure. *J Membr Sci* 2012;415–416:328–35.
- [120] Matsuka M, Braddock RD, Agranovski IE. Numerical study of hydrogen permeation flux in ytterbium doped strontium cerate and thulium doped strontium cerate (II). *Math Comput Simul* 2009;79:2713–23.
- [121] Song S-J, Wachsmann ED, Dorris SE, Balachandran U. Defect chemistry modeling of high-temperature proton-conducting cerates. *Solid State Ionics* 2002;149:1–10.
- [122] Poulsen FW. Method for calculating ionic and electronic defect concentrations in proton containing perovskites. *J Solid State Chem* 1999;143:115–21.
- [123] Norby T, Haugsrud R. Dense ceramic membranes for hydrogen separation. In: Sammells AF, Mundschauf MV, editors. *Nonporous inorganic membranes*. Weinheim: WileyVCH; 2006. p. 1–48.
- [124] Zhang Q, Zhu Z, Liu T, Liu W. Modeling of hydrogen permeation for Ni–BZCY asymmetric membrane. *J Membr Sci* 2013;437:196–204.